# 28. Multiple Materials Melting (Metals)

## Part of Experiment MA-150*

*L. I. Ivanov,[a] V. N. Kubasov,[a] V. N. Pimenov,[a] K. P. Gurov,[a] E. V. Demina,[a] Yu. S. Malkov,[a] and V. M. Lazarenko[a]*

### INTRODUCTION

Microgravity in space can be used to develop new technological processes for manufacturing materials. Weightlessness may be particularly beneficial in metallurgical synthesis of the so-called compound materials; i.e., materials composed of a meltable matrix and a heavy, more refractory second phase. The second-phase distribution for the solid-state components can be predetermined on Earth, and this distribution should remain unchanged after the matrix has been melted in conditions of "ideal" weightlessness.

Such materials systems are difficult to synthesize on Earth because of "weight" segregation of the elements, which results in a separation of the constituents in a molten-state matrix. It is believed that compound materials obtained in conditions of weightlessness possess unique physical, electrical, and other properties. Study of microgravity melting and solidification is of particular interest, both scientific and practical, for powdered metals and for alloys containing eutectics.

Equally interesting is the question of conducting basic scientific experiments under the weightless conditions of a space flight. For example, the study of laws governing mutual diffusion and growth of intermetallic phases within the diffusion area upon the interaction of solid and liquid metals is of great value for solid-state physics. The physical characteristics of diffusion processes can be investigated more effectively in a microgravity environment because of the much lower convection of space-molten metals compared to Earth-molten metals. The kinetics of these processes and the phase formation in tertiary systems represent yet other interesting points for study.

Therefore, the objectives of the metallic materials part of the Multiple Materials Melting Experiment were to investigate the effects of weightlessness on the following.

1. The feasibility of a metallurgical method of synthesizing compound materials with a predetermined distribution of constituents based on metals with significantly different specific gravities. Aluminum (Al) was chosen as a matrix and tungsten (W) was chosen as a "heavy" component.
2. The mutual diffusion and formation of intermetallic phases as a result of interaction of a meltable matrix (Al) and hard, refractory inclusions (W).
3. The melting and solidification of powdered Al.

Additional studies were made on microgravity melting and solidification of copper aluminum (CuAl) eutectic alloy as it interacts with Al, as well as on the diffusion and formation of intermetallic phases in the tertiary system of solid W, solid rhenium (Re), and liquid Al.

*The Multiple Materials Melting Experiment is one of the five experiments that incorporated joint activities between the U.S. and U.S.S.R. crews. The joint U.S.-U.S.S.R. designation was "Experiment AS-3." The "germanium-silicon solid solutions" part of the experiment is reported in section 29.

[a]Institute for Metallurgy, U.S.S.R.

## EXPERIMENTAL METHOD AND SAMPLE ANALYSIS

The starting composite material prepared for melting in space was an Al cylinder (fused from pellets) 8 mm in diameter and 9 mm high. A rod composed of special WRe alloy (rhenium content ≈30 wt%), 2 mm in diameter and 4.5 mm high, was fused into the upper part of the Al cylinder along its axis of gravity. Seven W balls (round samples with an average diameter of approximately 1 mm) were fused into the lower part of the cylinder along the plane perpendicular to the cylinder axis. Only high-purity metals were used for sample preparation. Before fusing, the material surfaces were carefully cleaned to remove any possible contaminants.

Samples prepared in this manner were wrapped in aluminum foil and placed in capped graphite crucibles. The crucibles were loaded into quartz ampoules, which were outgassed to approximately 0.133 $N/m^2$ (0.001 mmHg) and sealed. Figure 28-1 is an X-ray photograph of one of these ampoules.

The ampoules containing Al powder, obtained by crushing the solid Al sample, were prepared in the same manner. In addition to Al powder, each ampoule contained small pieces of CuAl eutectic alloy (mean diameter, ≈2 mm) that were insulated from the Al by aluminum foil. Three ampoules for each material were tested in conditions of weightlessness.

Similar samples were prepared for identical ground-based simulation tests. The specimens tested in flight were identified by the following numbers: MA-150-16, MA-150-17, and MA-150-18; the simulation samples were MA-150-9, MA-150-11, and MA-150-12. This report presents the experimental results for flight samples 16 and 17 as well as for ground-based samples 9, 11, and 12.

Both flight and ground-based samples were melted in a multipurpose electric furnace (sec. 21). The ampoules and sample materials were loaded in hermetically sealed cartridges. A disassembled view of the cartridge components is shown in figure 28-2. The fireproof cases used for transporting the cartridges onboard the Soyuz spacecraft are shown in figure 28-3.

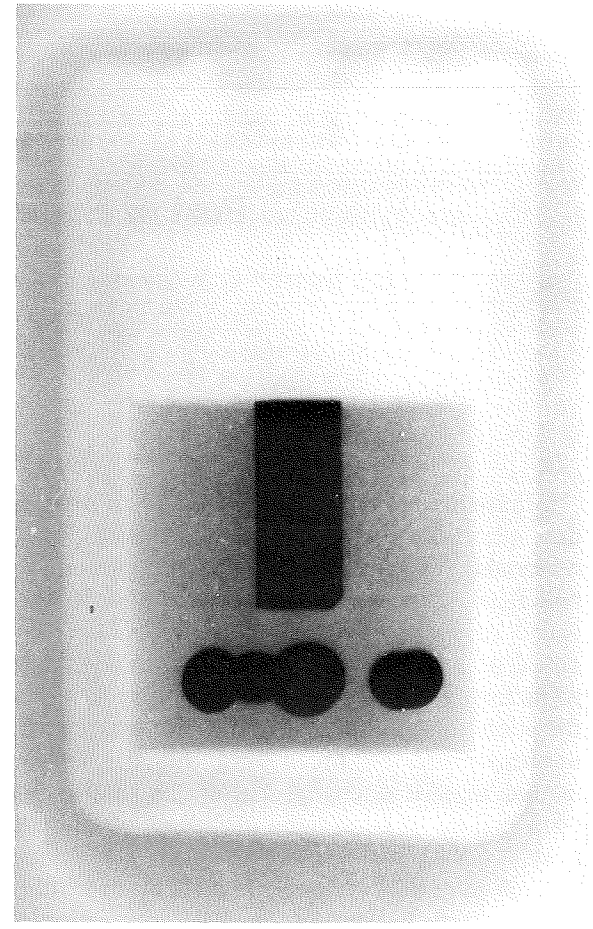

FIGURE 28-1.—X-ray photograph of ampoule containing a mixture of Al and W and WRe alloy. The balls are W; the rod is alloy.

Figure 28-4 is an X-ray photograph of flight cartridges showing the relative positions of compound material, powdered Al, and eutectics (also the germanium silicon crystals discussed in sec. 29). Figure 28-5 shows the thermal profile for the sample processed in flight. The same conditions were applied to ground-based processing.

After completion of the experiment, the ampoules and crucibles were first X-rayed for quick-look examination and then opened. The crucibles with compound material ingots were cut perpendicularly to the crucible axis.

Metallographically polished sections containing WRe rods, or W balls in cross section, were

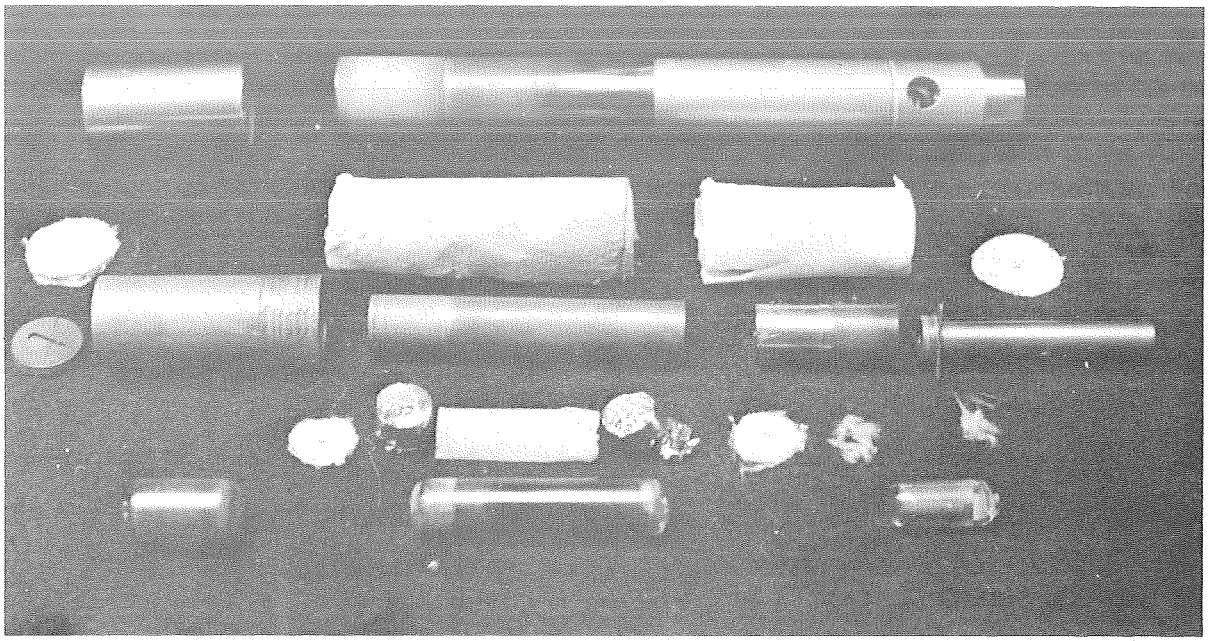

FIGURE 28-2.—Disassembled view of cartridge and ampoule with material specimen.

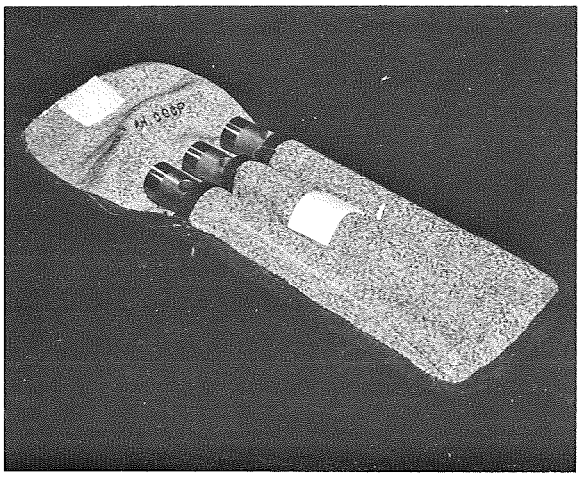

FIGURE 28-3.—Flight cartridges in transport case made of nonflammable cloth.

then prepared. Metallographic sections were also prepared from the pieces of eutectics. In etching the eutectic alloy sections, the following agents were used: 2.5 ml of nitric acid ($HNO_3$), 2 ml of hydrogen chloride (HCl), 1.5 ml of hydrogen fluoride (HF), and 94 ml of water ($H_2O$).

The polished sections were examined by means of optical microscopy, electron probe microanalysis (ref. 28-1), and electron scanning microscopy.

Phase composition of the microsections was determined by quantitative local X-ray spectral analysis (refs. 28-2 to 28-5). Based on the technique described in reference 28-2, the weight concentration $c_i$ of the $i$-th (heavier) component in a binary system is determined by

$$c_i = f_i^{(1)} f_i^{(2)} \frac{I_i}{I_{io}} \tag{28-1}$$

where $I_i$ and $I_{io}$ are the measured intensities of the characteristic radiation for the sample and for the standard, respectively; $f_i^{(1)}$ is the atomic number correction that considers different stopping power and different incident electron scattering for the sample and for the standard; $f_i^{(2)}$ is the absorption correction that considers the difference in absorption of the excited characteristic radiation for the

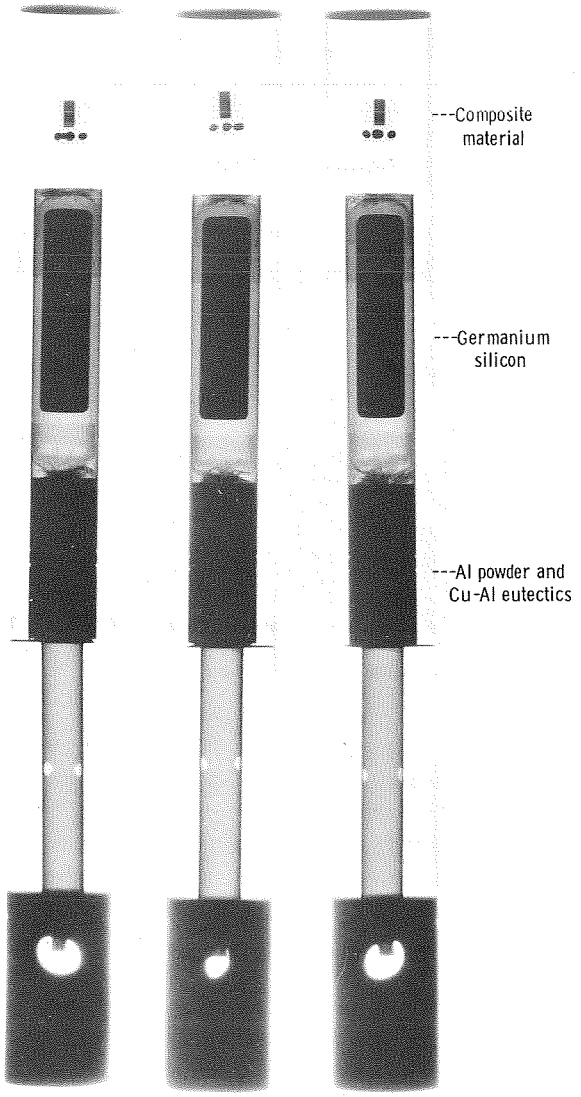


FIGURE 28-4.—X-ray photograph of flight cartridges MA-150-16, MA-150-17, and MA-150-18.

sample and the standard. These corrections are defined by

$$f_i^{(1)} = \frac{1 + 2\delta_i\left(1 - \beta^{-n}\right)}{1 + 2\delta_i^*\left(1 - \beta^{-n}\right)} \qquad (28\text{-}2)$$

$$f_i^{(2)} = \frac{1 + \alpha E_o^n \tau_i^*\left(1 - \beta^{-n}\right)\operatorname{cosec}\theta}{1 + \alpha E_o^n \tau_{ii}\left(1 - \beta^{-n}\right)\operatorname{cosec}\theta} \qquad (28\text{-}3)$$

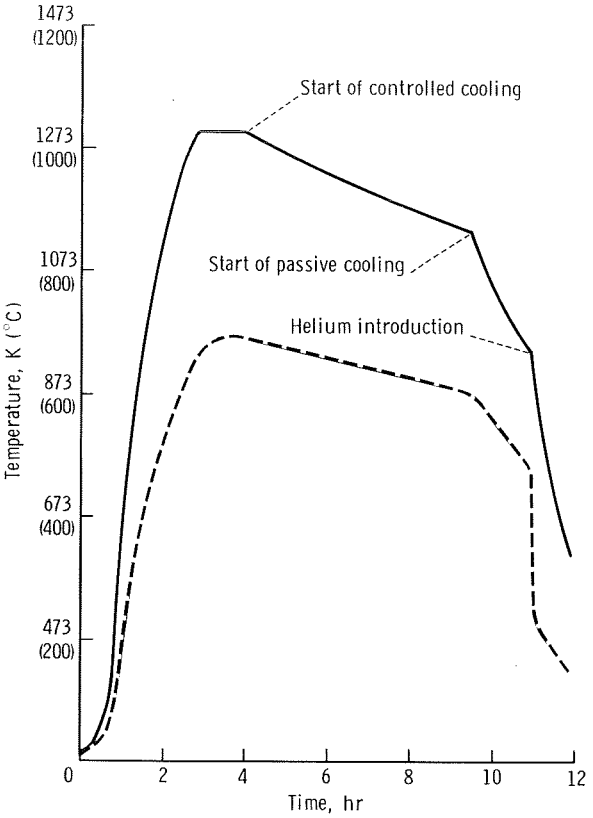


FIGURE 28-5.—Temperature-time profile of microgravity processing. The solid line indicates W-Al and W-Al-Re systems and the dashed line indicates powdered Al and CuAl eutectics.

where

$\delta_i^* = \sum_k c_k \delta_k$

$\delta_i$ = electron backscattering factor for the $i$-th element

$\beta = E_o/E_i$

$E_o$ = initial electron energy corresponding to accelerating voltage

$E_i$ = excitation energy of the studied radiation

$\tau_i^* = \sum_j c_j \tau_{ij}$

$\tau_{ij}$ = mass coefficients of the $i$-th radiation absorption by the $j$-$m$-th element in the sample

$\theta$ = angle of departure of radiation from the surface

$\alpha$ = dimensionless parameter equal to $3.33 \times 10^{-6}$ (ref. 28-2) provided that $E_o$ and $E_i$ are given in kiloelectronvolts

and parameter $n$ is assumed to be 1.62.

However, using methods previously described (refs. 28-3 to 28-5), atomic number and absorption corrections are determined for the ratio

$$c_i = f_i^{(1)} f_i^{(2)} f_i^{(3)} \left(I_i / I_{io}\right) \tag{28-4}$$

Here, in contrast to the other methods (ref. 28-2), the atomic number correction consists of two corrections: stopping power $f_i^{(1)}$ and electron backscattering $f_i^{(2)}$ and where $f_i^{(3)}$ is the absorption correction. These corrections are calculated from

$$f_i^{(1)} = \frac{\sum_k c_k \frac{Z_k}{A_k} \ln\left(0.585 \frac{E_o + E_i}{J_k}\right)}{\frac{Z_i}{A_i} \ln\left(0.585 \frac{E_o + E_i}{J_i}\right)} \tag{28-5}$$

$$f_i^{(2)} = \frac{1/R_i^*}{1/R_i} \tag{28-6}$$

$$f_i^{(3)} = \frac{\left(1 + \frac{\chi_i^*}{\sigma_i}\right)\left[1 + \frac{h_i \chi_i^*}{\left(1 + h_i^*\right)\sigma_i}\right]}{\left(1 + \frac{\chi_{ii}}{\sigma_i}\right)\left[1 + \frac{h_i \chi_{ii}}{\left(1 + h_i\right)\sigma_i}\right]} \tag{28-7}$$

where $E_o$ and $E_i$ = same values (in electronvolts) as those in reference 28-2

$Z_i$ = $i$-th element atomic number

$A_i$ = $i$-th element atomic weight

$J_i$ = 11.5 eV

$R_i^* = \sum_k c_k R_k$

$R_k$ = the electron backscattering factor for the $k$-th element (ref. 28-5)

$\chi_i^* = \text{cosec}\ \theta \sum_k c_k \tau_{ik}$

$\chi_{ii} = \tau_{ii} \text{cosec}\ \theta$

$\tau_{ik}$ = same values as those in reference 28-2

$h_i^* = \sum_k c_k h_k$

$h_k = 1.2 A_k / Z^2{}_k$

and $\sigma$ is the Lenard's modification factor associated with $E_o$ and $E_i$ by

$$\sigma = \frac{4.5 \times 10^5}{E_o^{1.65} - E_i^{1.65}} \tag{28-8}$$

where $E_o$ and $E_i$ are given in electronvolts.

The two methods used to calculate corrections for the systems under study yielded similar results. To determine the unknown concentration in the analyzed specimens, special averaged calibration curves were constructed from the calculation data $c_i = c_i(I_i/I_{io})$, where $i$ = W for the W-Al and W-Al-Re systems; and $i$ = Cu for the Cu-Al system. A calculation for the tertiary system (W-Al-Re) was made with the same method as that used for the W-Al system (ref. 28-2) because equalities $\tau_{WW} \approx \tau_{WRe}$, $\tau_{ReRe} \approx \tau_{ReW}$, $\tau_{WAl} \approx \tau_{ReAl}$, and $\tau_{AlW} \approx \tau_{AlRe}$ are valid for both W and Re, which are adjacent elements in the periodic table. Figure 28-6 is an example of a W-Al system calibration curve that was used to determine W concentration. In general, the system was analyzed along the lines W L$\alpha$ , Al K$\alpha$ (W-Al); W L$\alpha$ , Al K$\alpha$, Re L$\alpha$ (W-Al-Re); Cu K$\alpha$ , Al K$\alpha$ (Cu-Al); $E_o$ = 20 keV.

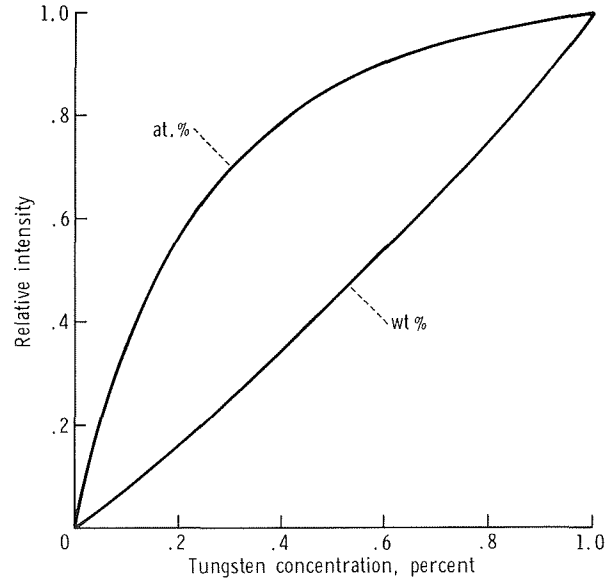


FIGURE 28-6.—Relative intensity of W L$\alpha$ radiation as a function of concentration for the W-Al system ($E_o$ = 20 keV).

## EXPERIMENTAL RESULTS

### Compound Materials

The X-ray photographs (fig. 28-7) of the ampoules and ingots for both ground-based and flight experiments show evidence that neither of the solidified materials preserved the initial structure (fig. 28-1). Also, the distribution of the refractory inclusions throughout the Al in the flight samples differed from that of the ground-based samples. In the flight samples, the W balls were distributed throughout the bulk of the materials. In the ground-based samples, the cylindrical rod was on the ingot surface and the W balls were at the bottom of the crucible (fig. 28-8). The space-grown ingot (fig. 28-7) is larger and has a different shape than the Earth-grown ingot. The end of the flight specimen at the bottom of the crucible is almost conical.

### Tungsten and Aluminum Matrix Interaction

The W specimens showed a certain distribution throughout the Al. Two patterns were discernible in cross section: an almost circular one and a horseshoelike pattern.

Examination of the specimens by electron scanning microscopy and X-ray spectral analysis

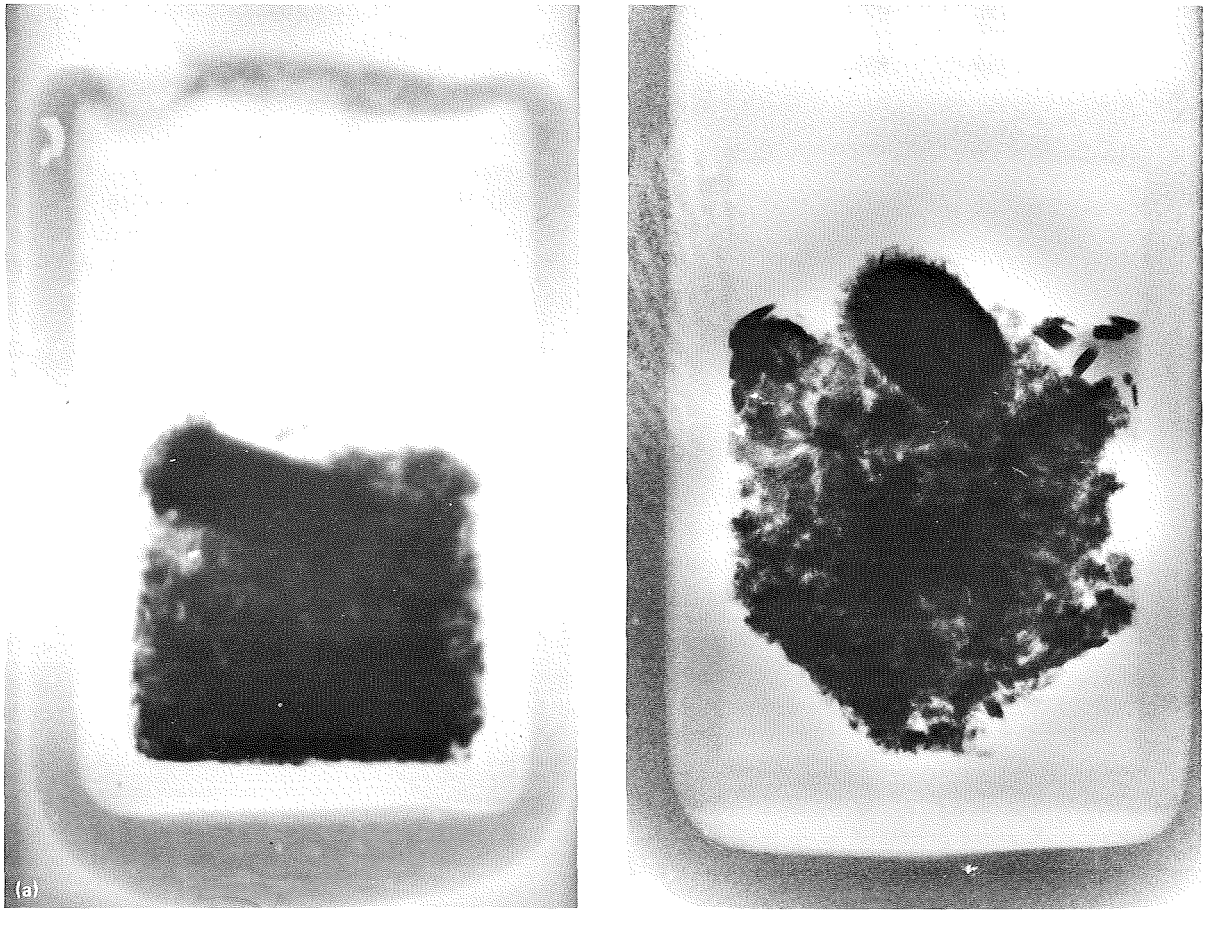


FIGURE 28-7.—X-ray photograph of ampoules with ingots. (a) Earth-grown sample MA-150-11. (b) Space-grown sample MA-150-17.

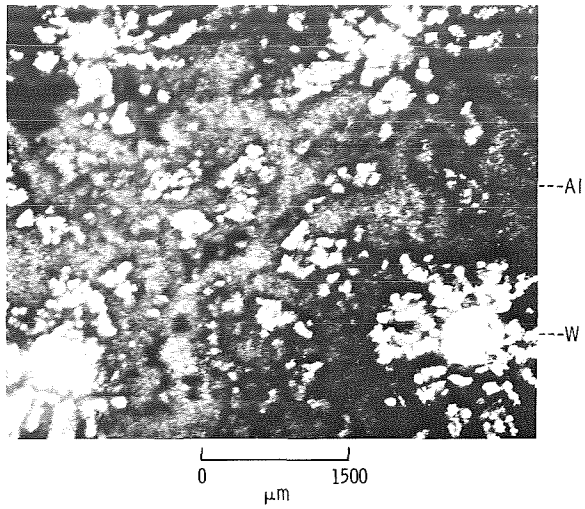


FIGURE 28-8.—Photomicrograph of a sectioned area of ground-based sample MA-150-12 in the plane passing through W samples near the bottom of the crucible.

revealed the existence of an area of interaction between W and Al composed entirely of intermetallic phases. The distribution of this interaction area across the ground and flight specimen sections is shown in figures 28-9 to 28-13. These figures show that the area, in all cases, is a diffusion layer that disintegrates farther from the W into individual, elongated and dentritic sections. The latter are usually separated from the main part (adjacent to W) of the diffusion layer by a layer of Al. The main bulk of the layer, as shown by quantitative X-ray spectral analysis, consists generally of three phases: $WAl_4$, $WAl_5$, and $WAl_{12}$. Phase boundary concentrations determined for zero-g conditions correspond within measurement accuracy to those determined for one-g conditions, and agree with the W-Al system phase diagram data (fig. 28-14).

The distribution of intensity of the characteristic W L$\alpha$ radiation for two different sections of the flight specimen diffusion layer is shown in figure 28-15. This figure indicates that, in one section of the diffusion layer (fig. 28-15(a)), phase distribution conforms to the laws of phase growth resulting from mutual diffusion (ref. 28-7) and that, in the second section (fig. 28-15(b)), these laws have not been followed. Ground-based specimens exhibit a similar behavior. It is interesting to note that the diffusion layer in ground-based and flight specimens had an extremely ragged front at the boundary with Al and a better defined front at the boundary with W (figs. 28-9 and 28-11 to 28-13). The $WAl_5$ phase comprises the main bulk of the layer; it constitutes a base for the "elongated" areas (figs. 28-9 to 28-13). The $WAl_4$ and

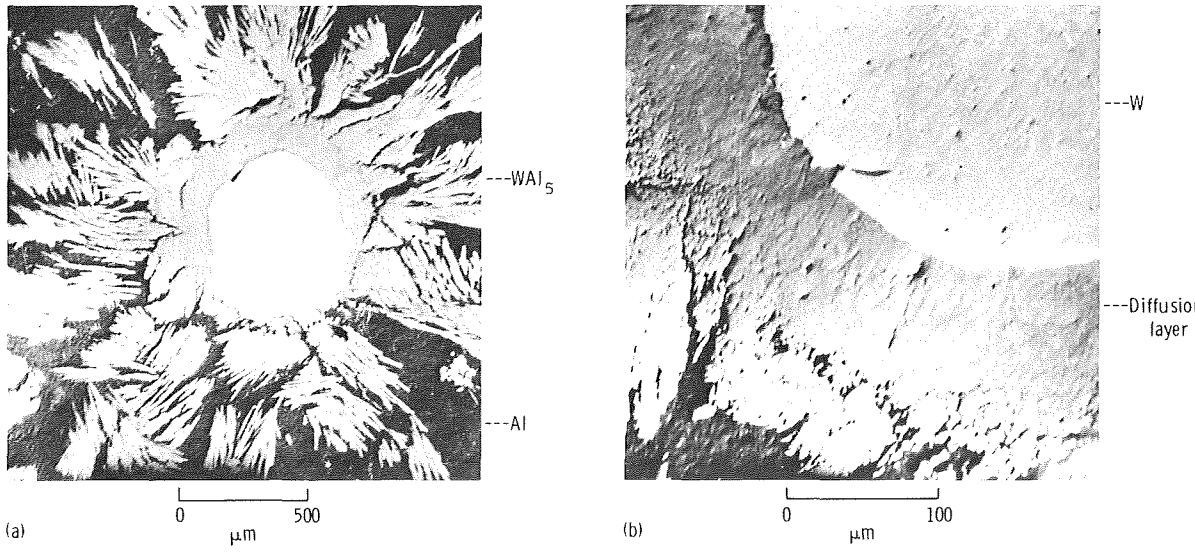


FIGURE 28-9.—Electron probe scanning of a sectioned area of ground-based sample MA-150-12. (a) $WAl_5$ phase region. (b) Tungsten/diffusion layer interface.

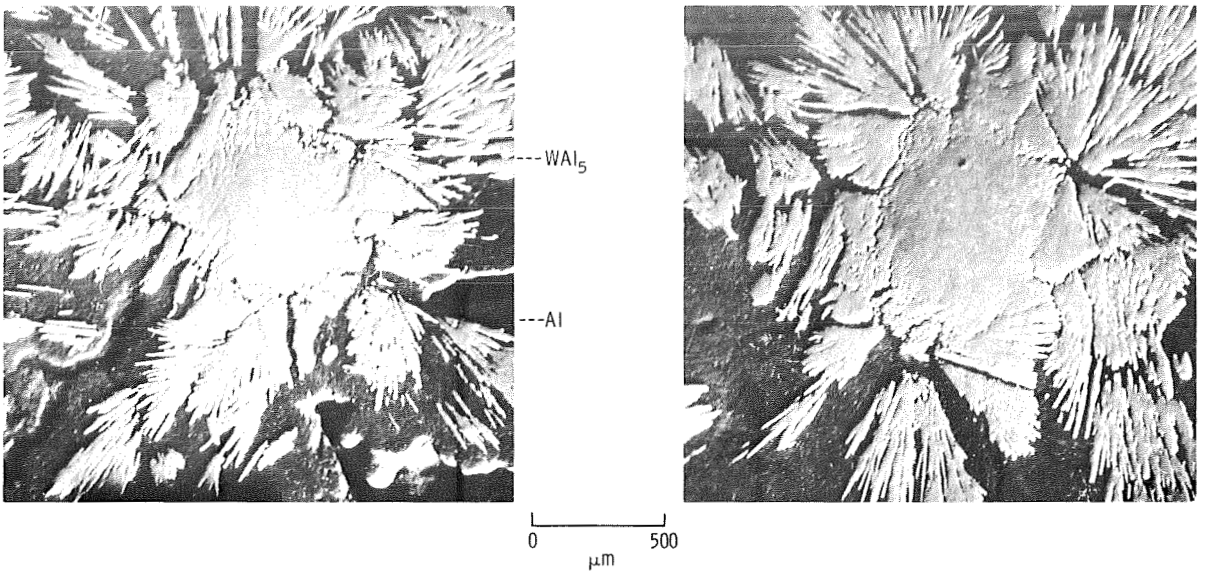


FIGURE 28-10.—Electron probe scanning of two sectioned areas of ground-based sample MA-150-12. Shear plane passes above the W specimens and cuts across the diffusion layer.

$WAl_{12}$ phases are generally not as thick and do not occur in some parts of the layer. Generally, the layer displays a considerable variation in phase thickness and an extreme raggedness of interphase boundaries.

Interestingly, the $WAl_{12}$ phase in the flight sample (MA-150-16) has a crystalline faceting (fig. 28-12), a fact not observed in ground samples. Furthermore, in ground-based and flight samples, all these phases occur as individual fragments

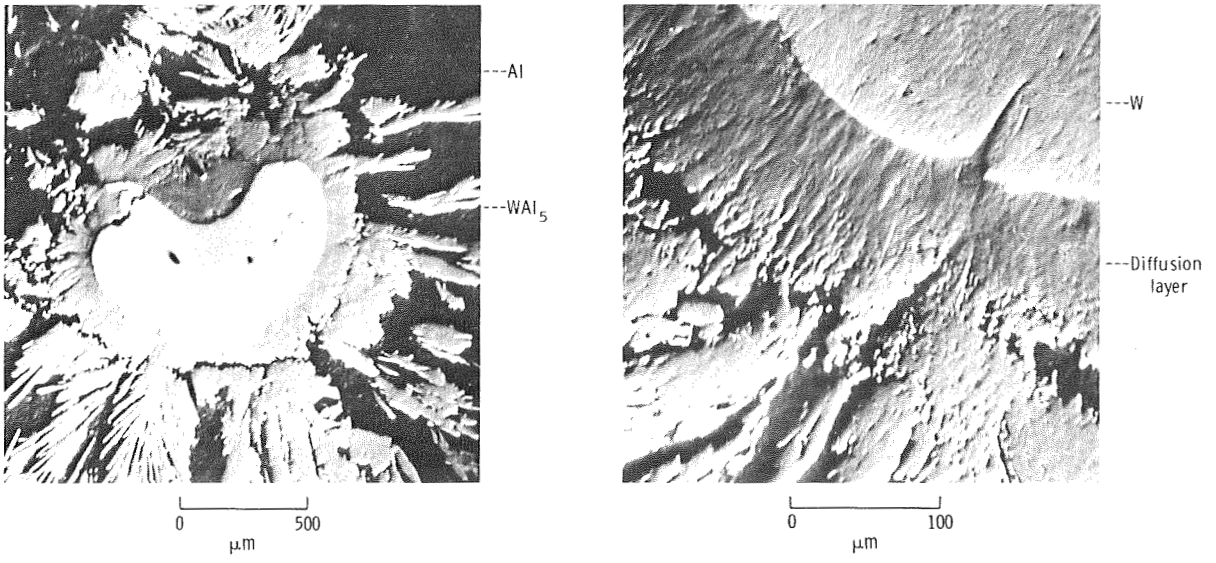


FIGURE 28-11.—Electron probe scanning across a sectioned area of ground-based sample MA-150-12.

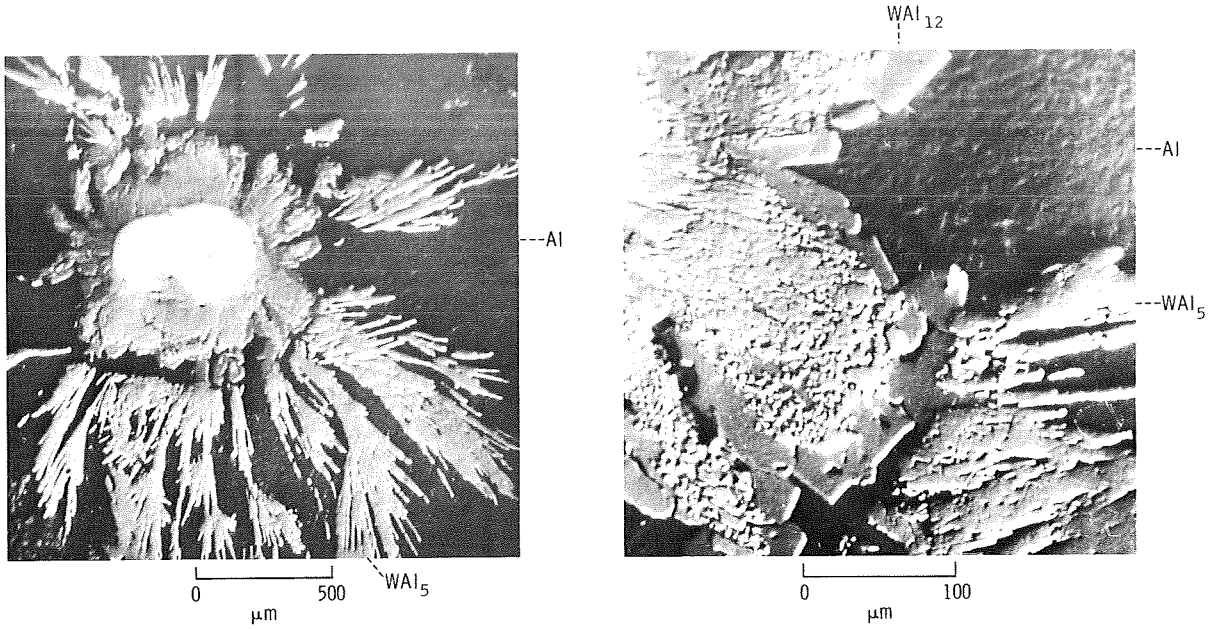


FIGURE 28-12.—Electron probe scanning across a sectioned area of flight sample MA-150-16.

throughout different parts of the ingot within the studied plane of the section. Fragments of $WAl_4$ and $WAl_{12}$ phases are irregularly shaped, whereas the $WAl_5$ phase occurs usually as needlelike fragments (fig. 28-14).

The sectioned areas of ground-based and flight samples, lying far from the diffusion layer and containing the $WAl_5$ phase, are shown in figures 28-16 to 28-19. An analysis has shown that the "needles" of this phase in flight specimens are

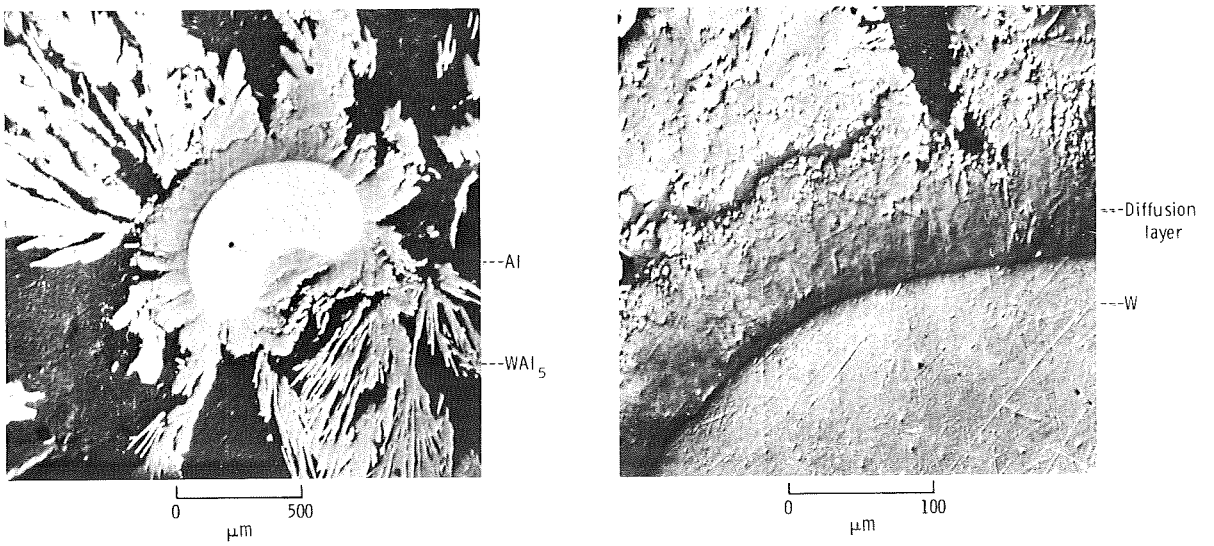


FIGURE 28-13.—Electron probe scanning of a sectioned area of flight sample MA-150-17.

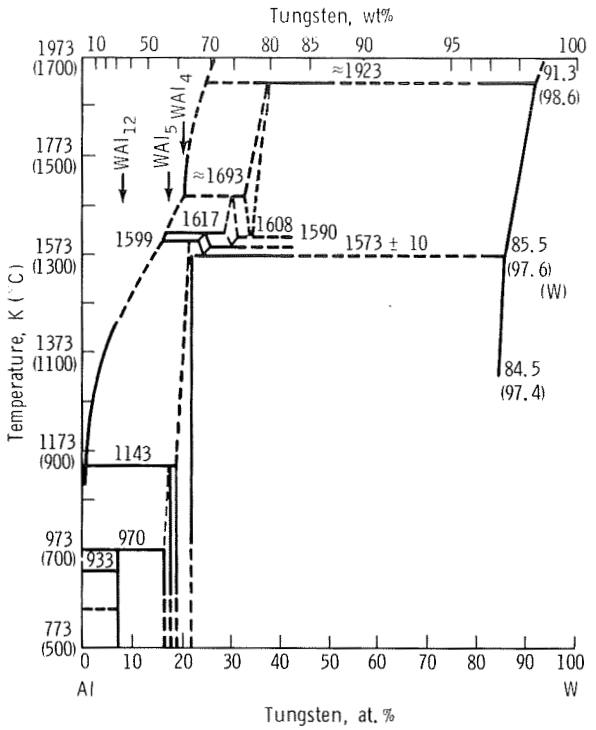


FIGURE 28-14.—Constitutional diagram of the W-Al system based on data from reference 28-6.

thinner and somewhat less disoriented than in ground specimens. However, individual, separated needles of the $WAl_5$ phase are encountered more frequently in ground-based specimens (fig. 28-18).

For sections of ground-based and flight samples containing W inclusions, microhardness $H$ was measured for the Al matrix, for W inclusions, and for phases formed as a result of interaction of solid-state W and liquid Al. The results are summarized in table 28-I. The table indicates that the values of microhardness in the samples are compatible within the limits of measurement error. The greatest hardness was determined for the diffusion layer $WAl_5$ phase. (Hardness of the $WAl_4$ phase was not measured because of its low thickness in the diffusion layer.)

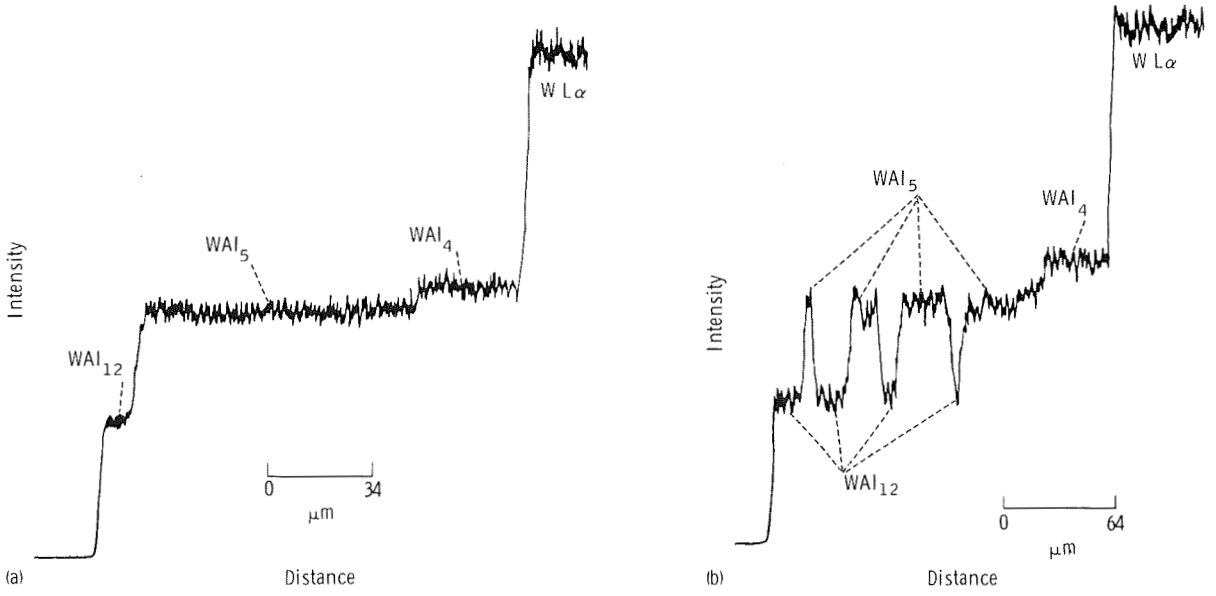


FIGURE 28-15.—Recordings of two types of intensity distributions of characteristic W Lα radiation for two different sections of the W/Al diffusion layer for sample MA-150-17. (a) Section 1. (b) Section 2.

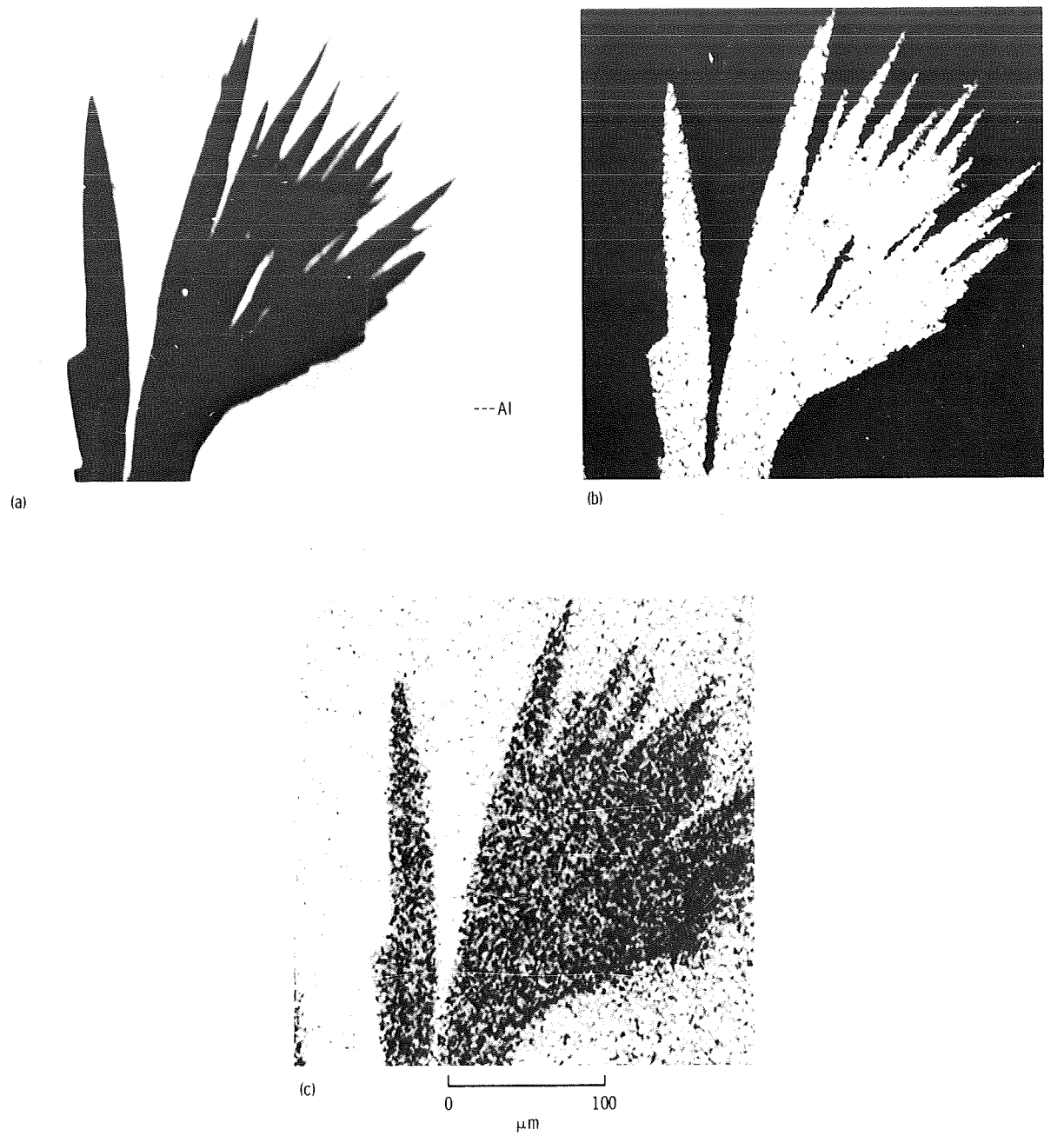


FIGURE 28-16.—Scanning of the $WAl_5$ phase in a section of ground-based sample MA-150-11. (a) Electron beam scanning. (b) Tungsten Lα radiation. (c) Aluminum Kα radiation.

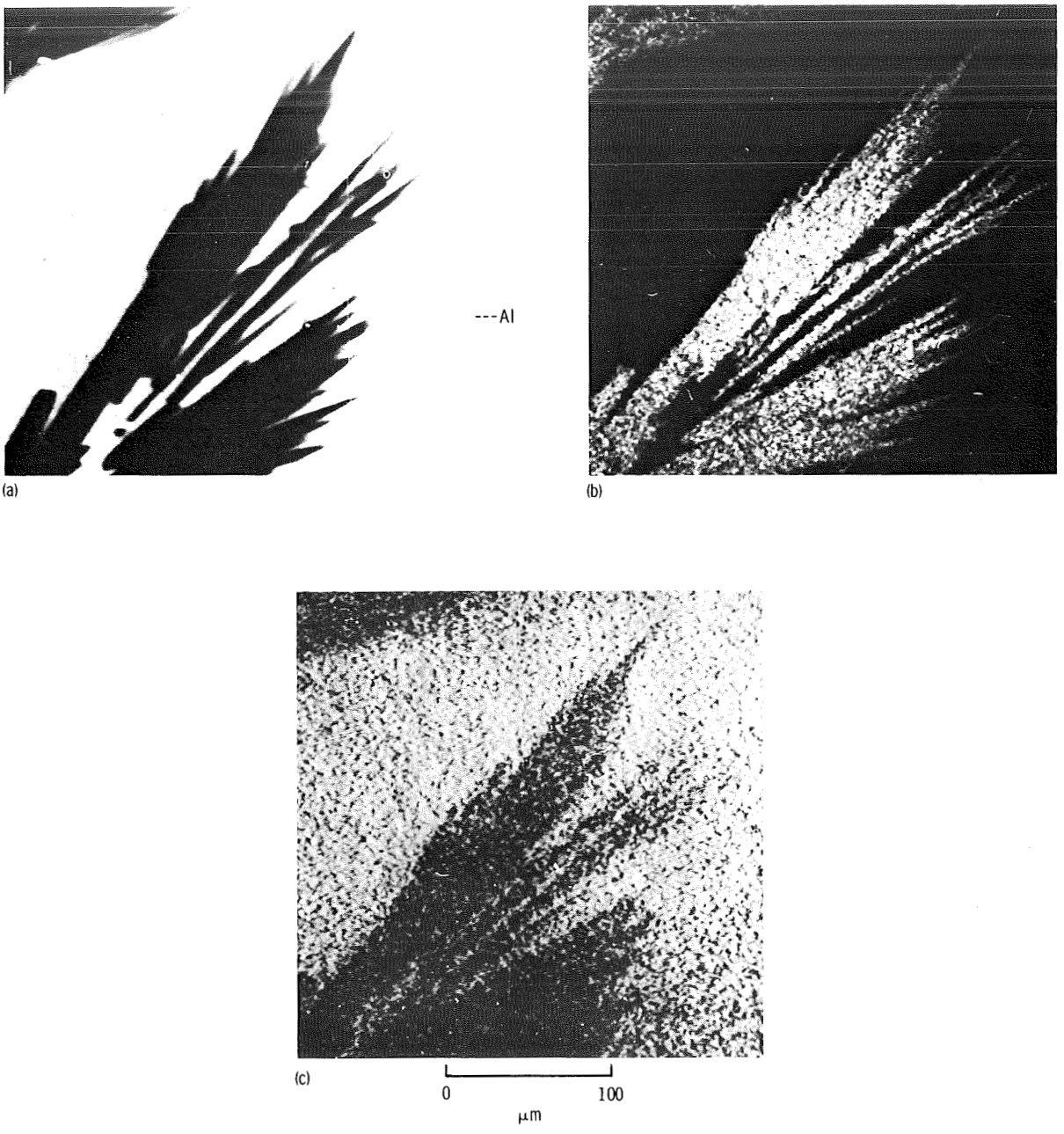


FIGURE 28-17.—Scanning of $WAl_5$ phase in metallographically polished flight sample MA-150-16. (a) Electron beam scanning. (b) Tungsten L$\alpha$ radiation. (c) Aluminum K$\alpha$ radiation.

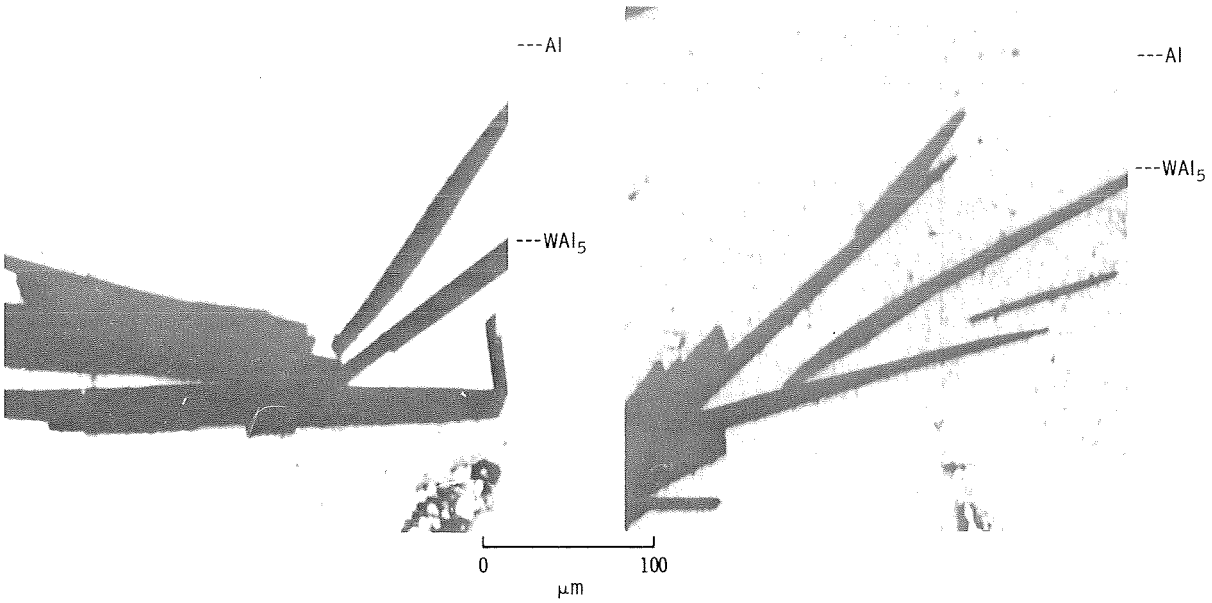


FIGURE 28-18.—Electron beam scanning across two sectioned areas of ground-based sample MA-150-11 containing the $WAl_5$ phase.

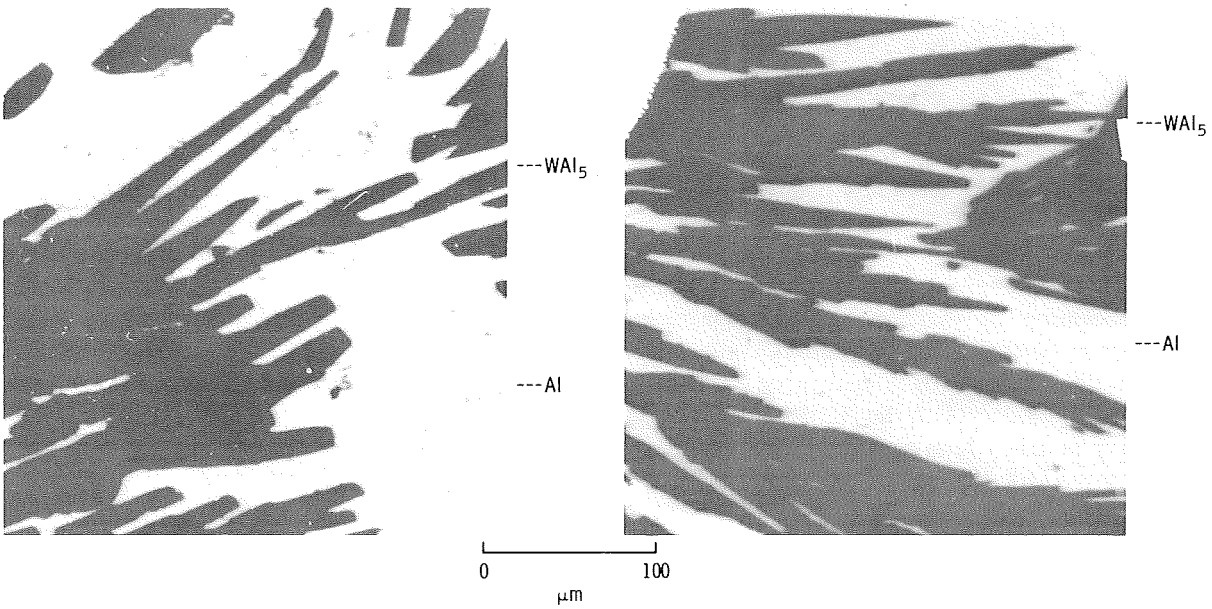


FIGURE 28-19.—Electron beam scanning of flight sample MA-150-16 in two sectioned areas containing the $WAl_5$ phase.

*TABLE 28-I.—Microhardness Measurement Results for Al Matrix, W Inclusions, and Interaction Phases*

| *Specimen* | *Phase* | *Microhardness H, kg/mm²* |
|---|---|---|
| MA-150-11 (ground-based) | W – ball-shaped | -- |
| | Al – matrix | 21 |
| | $WAl_5$ – needle-shaped | 500 |
| MA-150-12 (ground-based) | W – ball-shaped | 470 |
| | W – horseshoe-shaped | 500 |
| | Al – matrix | 21 |
| | $WAl_5$ – needle-shaped | 500 |
| | $WAl_5$ – diffusion layer | 550 |
| | $WAl_{12}$ – -- | 310 |
| MA-150-16 (flight) | W – horseshoe-shaped | 480 |
| | Al – matrix | 21 |
| | $WAl_5$ – needle-shaped | 470 |
| | $WAl_5$ – diffusion layer | 550 |
| | $WAl_{12}$ – -- | 390 |
| MA-150-17 (flight) | W – horseshoe-shaped | 480 |
| | Al – matrix | 21 |
| | $WAl_5$ – needle-shaped | 480 |
| | $WAl_5$ – diffusion layer | 550 |
| | $WAl_{12}$ – -- | 370 |

## Tungsten-Rhenium Alloy and Aluminum Matrix/Interaction

The section analysis revealed that an interface exists between starting alloy and Al along the entire length of the W-Re rod/matrix contact area (fig. 28-20). The front of this interface is more ragged at the boundary with the Al than at the boundary with the alloy, although the raggedness is approximately of the same type for flight and ground specimens (figs. 28-21 and 28-22).

The X-ray spectral analysis of different parts of the interface in polished sections showed it to be composed of two phases with irregular boundaries. The distribution of the intensity of the characteristic W L$\alpha$, Al K$\alpha$, and Re L$\alpha$ radiation in the examined sections is shown in figure 28-23. It is clear from the figure that the distribution of phases conforms to the laws governing their growth in the process of mutual diffusion in a tertiary system. The conversion of relative intensities into concentrations enabled the construction of concentration curves for the distribution of each constituent in the diffusion layer (fig. 28-24). The boundary concentration values for flight-sample phases correspond, within measurement accuracy, to the respective concentration values obtained for ground-based samples. Both samples show almost identical distribution of corresponding constituents within the same phases. Figure 28-24 also indicates that some difference in phase and diffusion layer thickness exists between flight and ground-based samples. However, the same variation in thickness was observed throughout different areas of the same sample (both flight and ground-based), although the phase adjacent to the alloy was invariably the one with the greatest thickness. In all cases, the X-ray spectral analysis

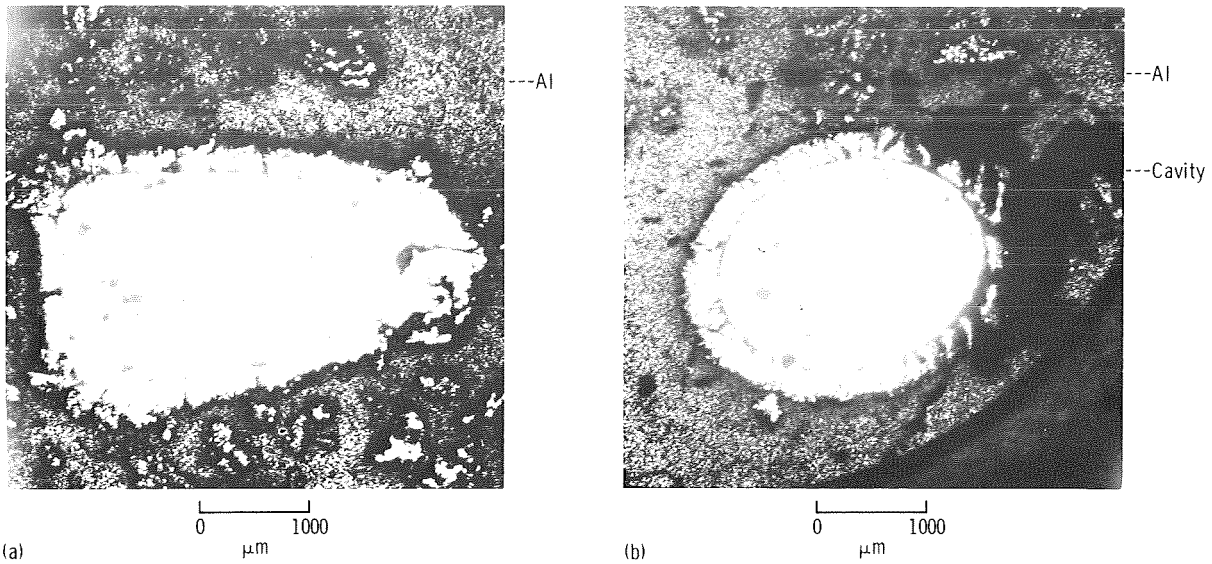


FIGURE 28-20.—Photomicrograph of metallographically polished sections. The WRe alloy and the adjacent diffusion layer are in the center. (a) Ground-based sample MA-150-11. (b) Flight sample MA-150-16.

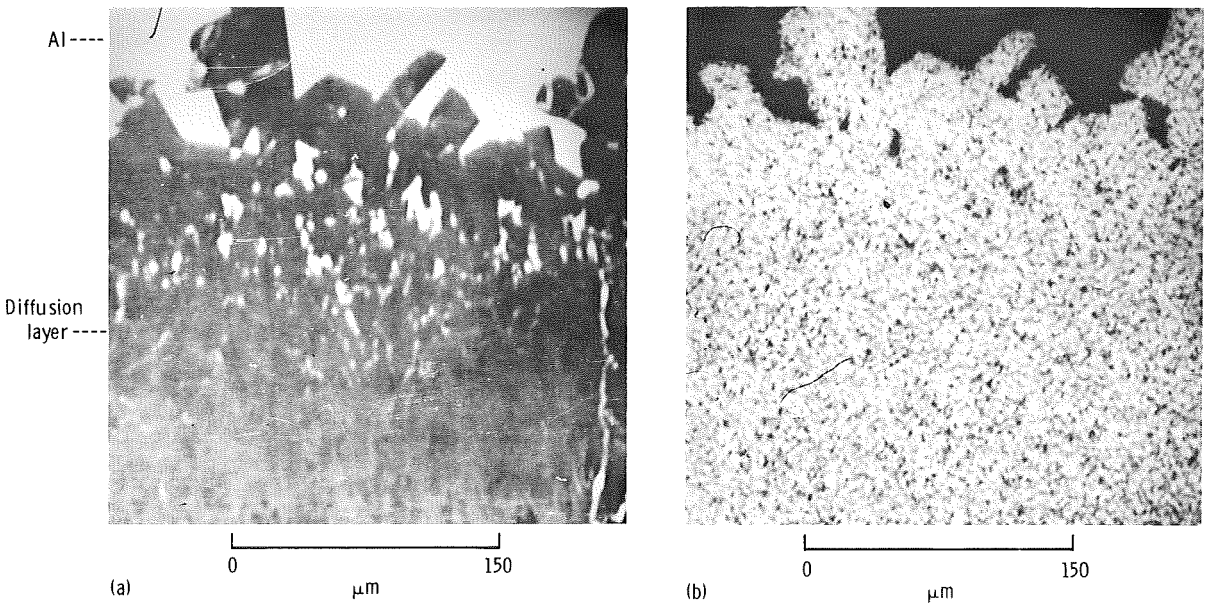


FIGURE 28-21.—Scanning of the diffusion layer in the ground-based sample MA-150-11. (a) Electron beam scanning. (b) Tungsten Lα radiation. (c) Aluminum Kα radiation. (d) Rhenium Lα radiation.

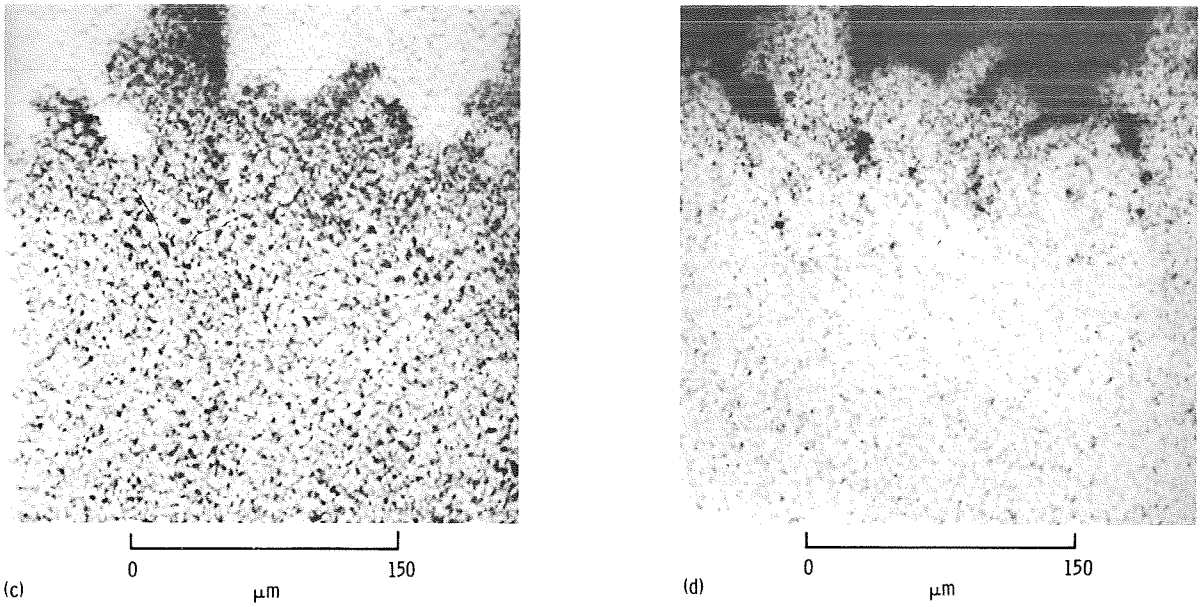


FIGURE 28-21.—Concluded.

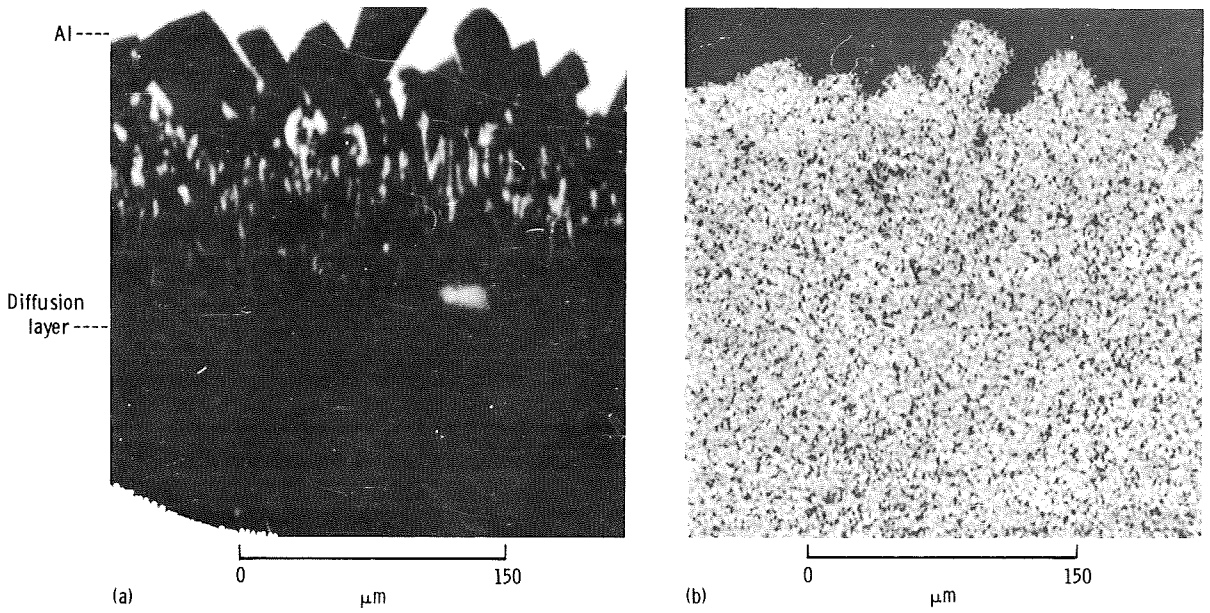


FIGURE 28-22.—Scanning of diffusion layer in flight sample MA-150-16. (a) Electron beam scanning. (b) Tungsten Lα radiation. (c) Aluminum Kα radiation. (d) Rhenium Lα radiation.

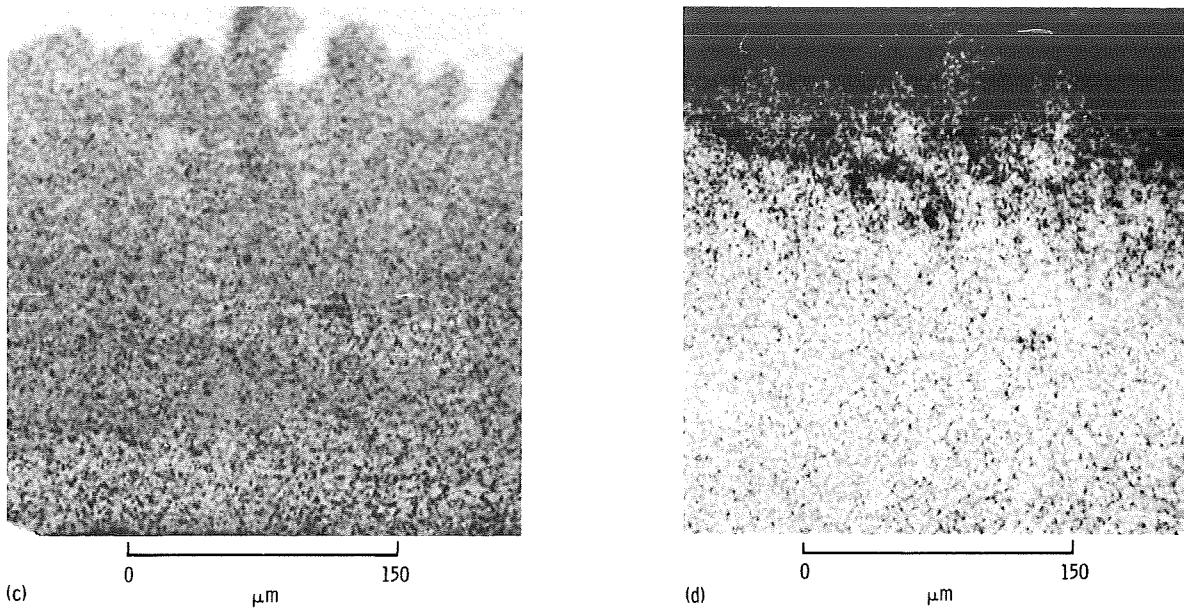


FIGURE 28-22.—Concluded.

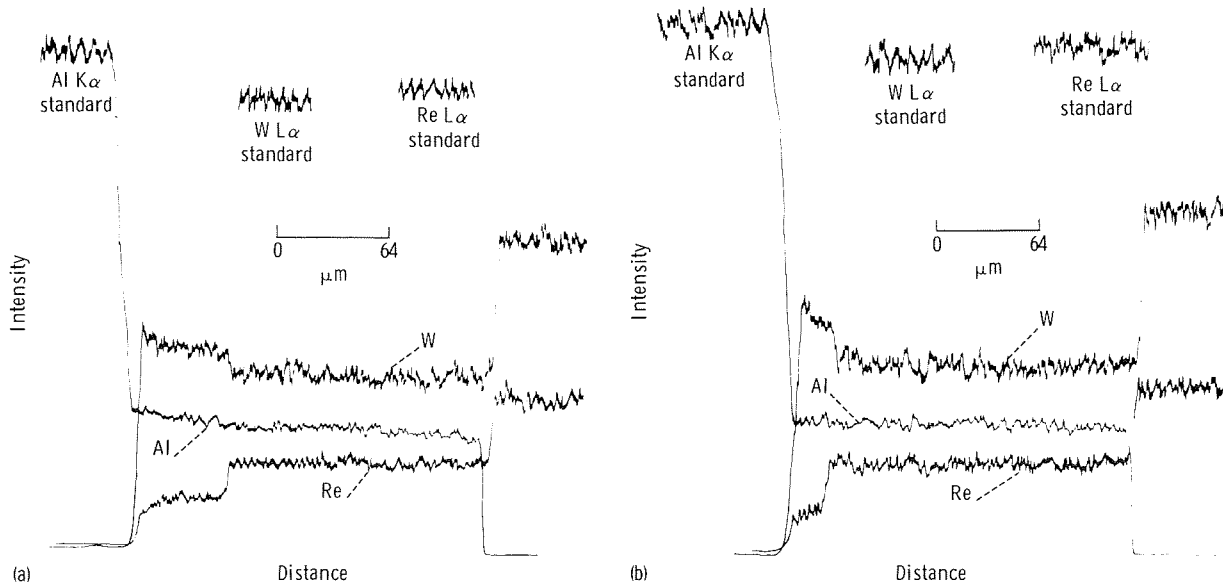


FIGURE 28-23.—Distribution of intensities of W $L\alpha$, Al $K\alpha$, and Re $L\alpha$ radiation throughout the diffusion layer. (a) Ground-based sample MA-150-11. (b) Flight sample MA-150-16.

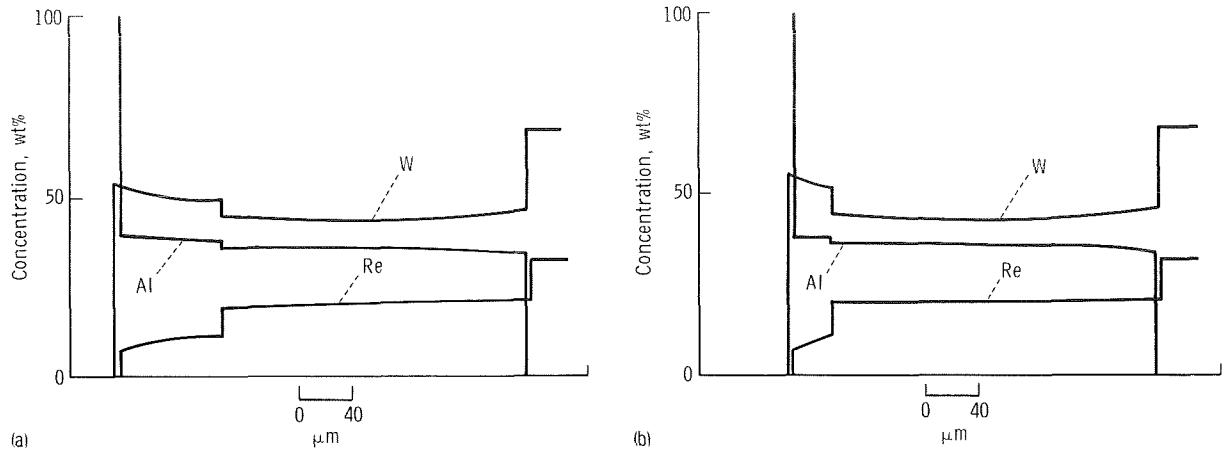


FIGURE 28-24.—Concentration curves showing distribution of W, Al, and Re in the diffusion layer. (a) Ground-based sample MA-150-11. (b) Flight sample MA-150-16.

revealed pure Al inclusions in the diffusion layer, located in the main near the boundary of the two phases (figs. 28-21 and 28-22). On the other hand, single fragments of tertiary phases, varying in size and shape, can be seen in different parts of the section of Al matrix. Examples of such chaotic dispersion of phases across sections are shown in figures 28-25 to 28-30. None of the fragments in the figures appear to be needle-shaped, as was the case with binary system W-Al. A quantitative analysis of a fairly large number of these fragments was made to determine their composition in the studied specimens. The results, averaged over several close values and normalized to 100 wt%, are shown in table 28-II.

In flight and ground-based specimens, the phase composition in different parts of sections is generally similar to that of the diffusion layers (fig. 28-24). However, one striking feature in flight specimen MA-150-16 is the presence of phase fragments with a higher Al content (more than 60 wt%). Examples of such Al-rich phases are presented in figures 28-29 and 28-30. No Al-rich phases were found in ground specimens. Furthermore, sample MA-150-11 contained fragments of phases composed of W, 45; Al, 38, and Re, 17

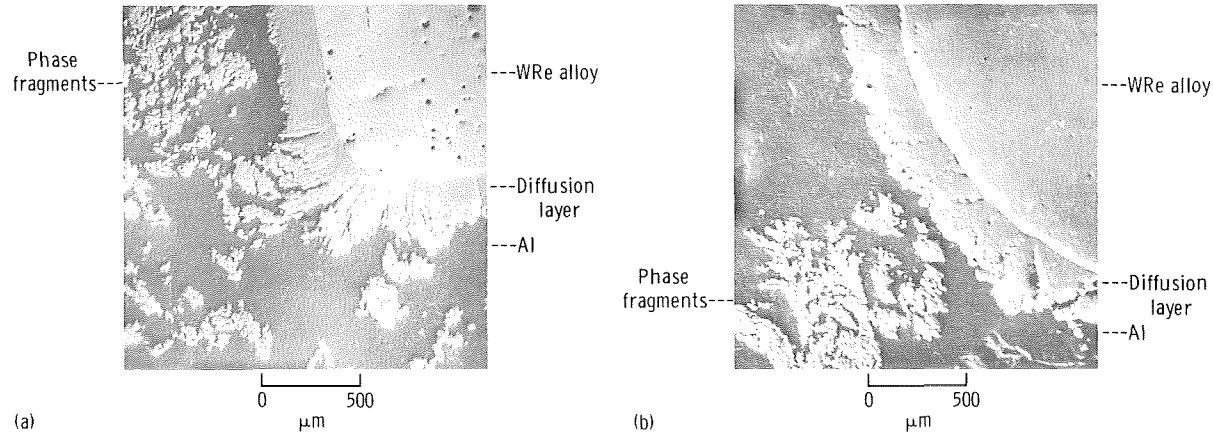


FIGURE 28-25.—Electron probe scanning of metallographically polished sections. (a) Ground-based sample MA-150-11. (b) Flight sample MA-150-16.

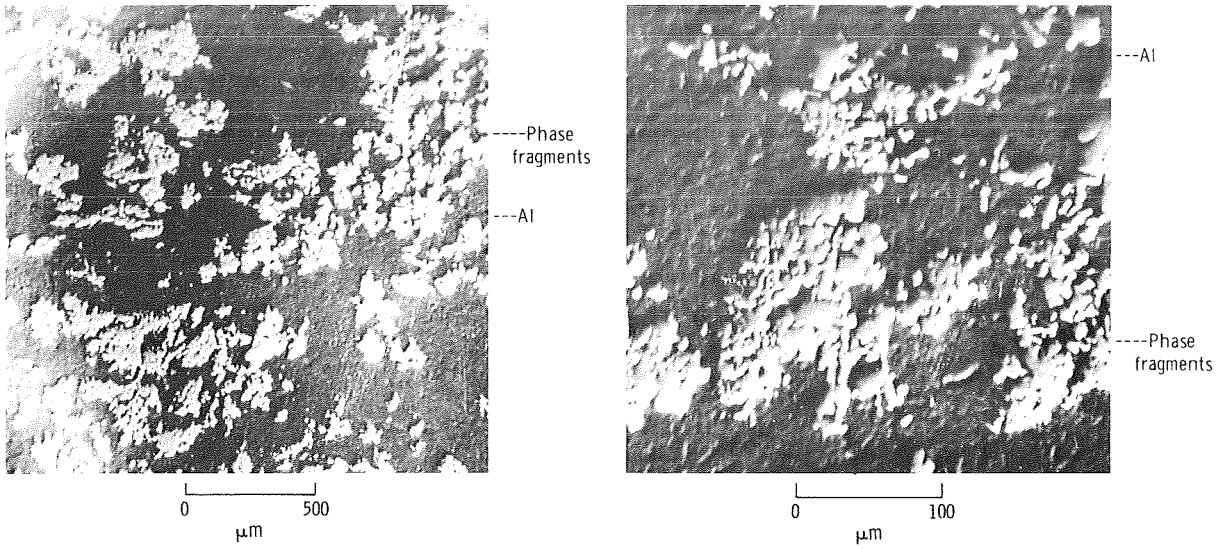


FIGURE 28-26.—Electron probe scanning across a sectioned area of flight sample MA-150-16 containing fragments of W-Al-Re system phases.

*TABLE 28-II.—Phase Composition*

| *Sample* | *Phase composition, wt%* | | |
|---|---|---|---|
| | *W* | *Al* | *Re* |
| MA-150-11 (ground-based) | 55 | 39 | 6 |
| | 53 | 38 | 9 |
| | 59 | 37 | 4 |
| | 45 | 38 | 17 |
| MA-150-12 (ground-based) | 55 | 37 | 8 |
| | 53 | 38 | 9 |
| | 58 | 37 | 5 |
| | 60 | 36 | 4 |
| MA-150-16 (flight) | 56 | 37 | 7 |
| | 58 | 39 | 3 |
| | 58 | 37 | 5 |
| | 60 | 37 | 3 |
| | 31 | 66 | 3 |
| | 33 | 64 | 3 |
| MA-150-17 (flight) | 56 | 37 | 7 |
| | 55 | 38 | 7 |
| | 59 | 39 | 2 |
| | 59 | 37 | 4 |

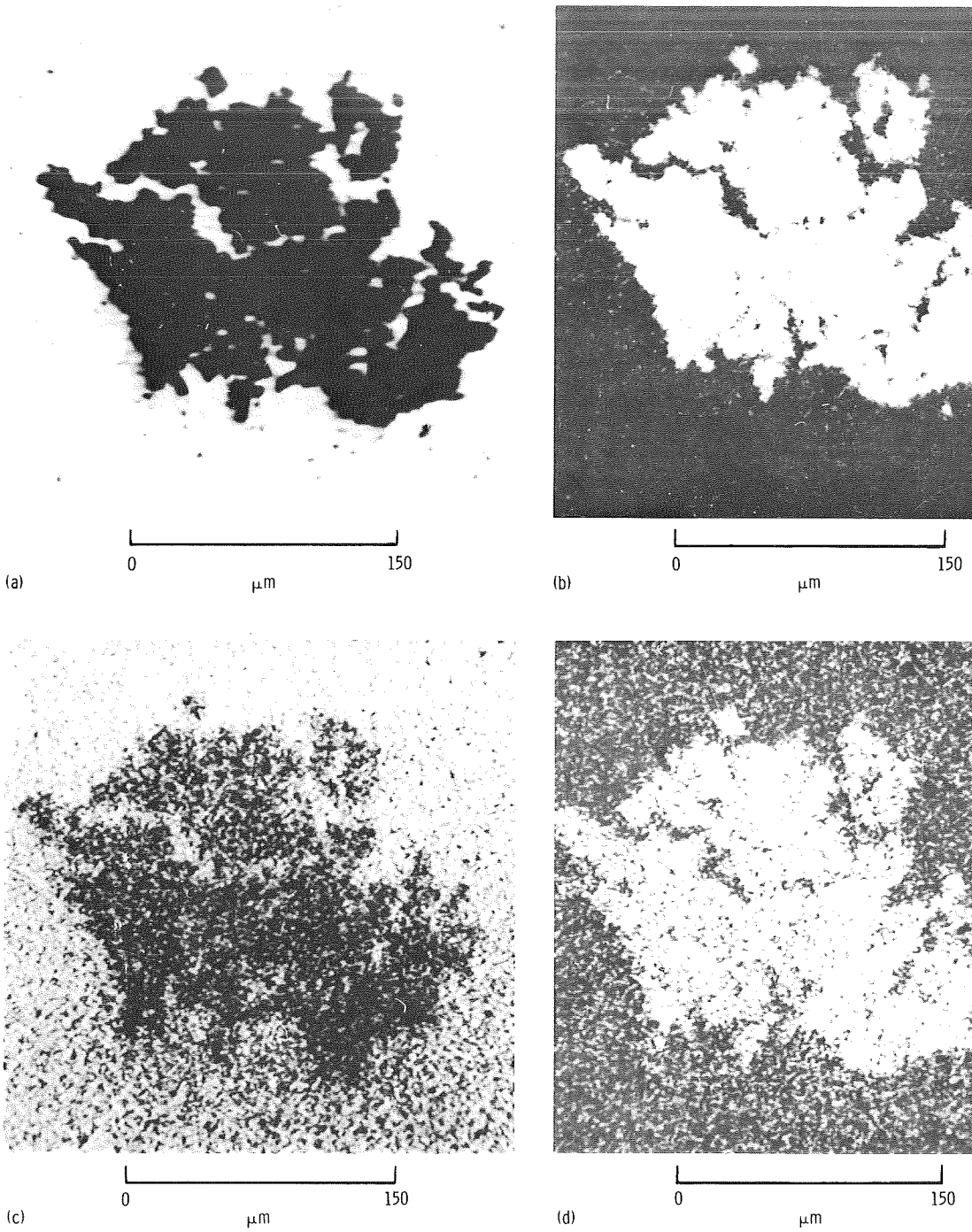


FIGURE 28-27.—Scanning of ground-based sample MA-150-11 in sectioned areas containing the W-Al-Re system phase. The W-Al-Re phase is shown in the center. (a) Electron beam scanning. (b) Tungsten L$\alpha$ radiation. (c) Aluminum K$\alpha$ radiation. (d) Rhenium L$\alpha$ radiation.

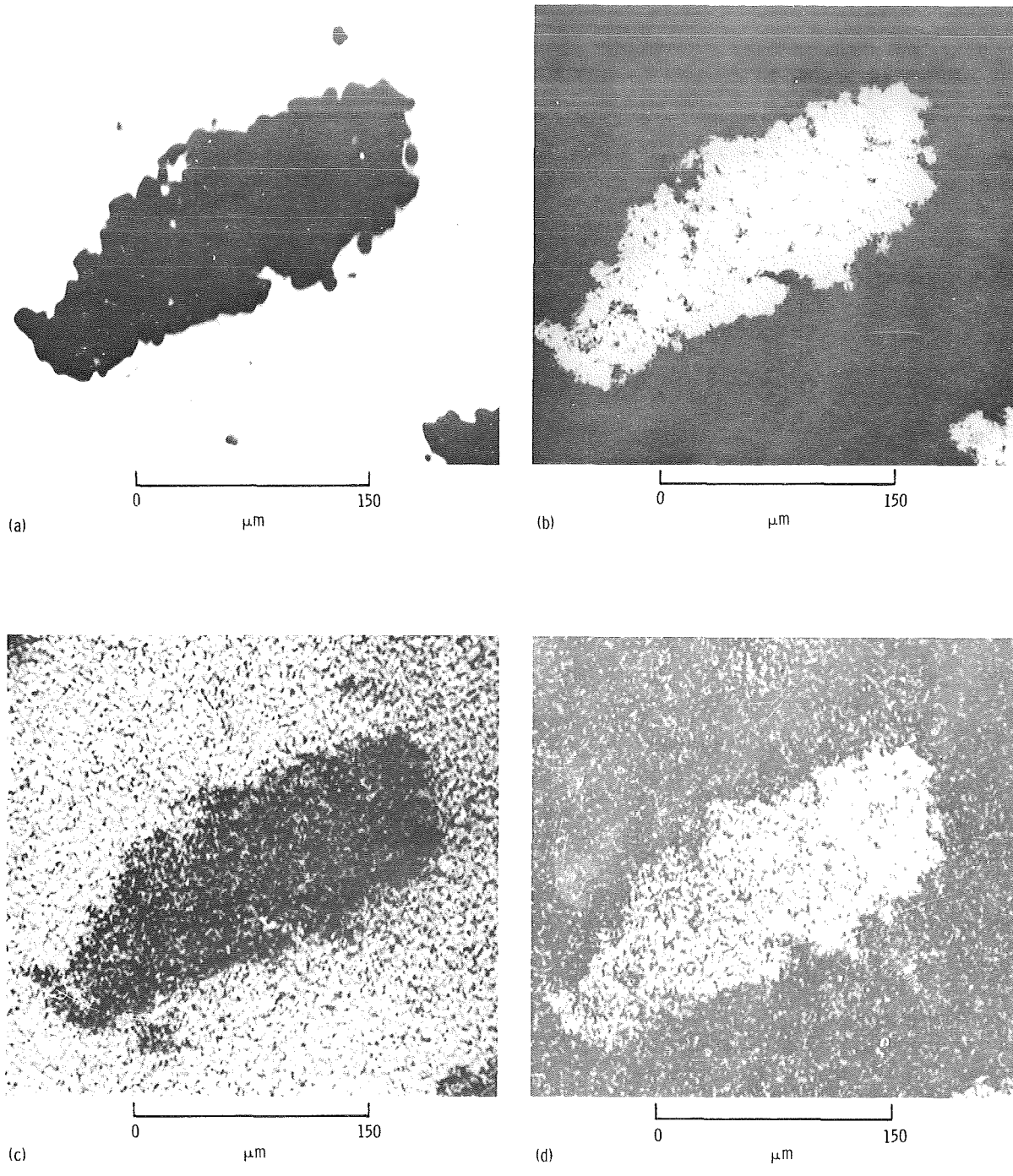


FIGURE 28-28.—Scanning of flight sample MA-150-16 in the sectioned areas containing the W-Al-Re system phase. The W-Al-Re phase is shown in the center. (a) Electron beam scanning. (b) Tungsten Lα radiation. (c) Aluminum Kα radiation. (d) Rhenium Lα radiation.

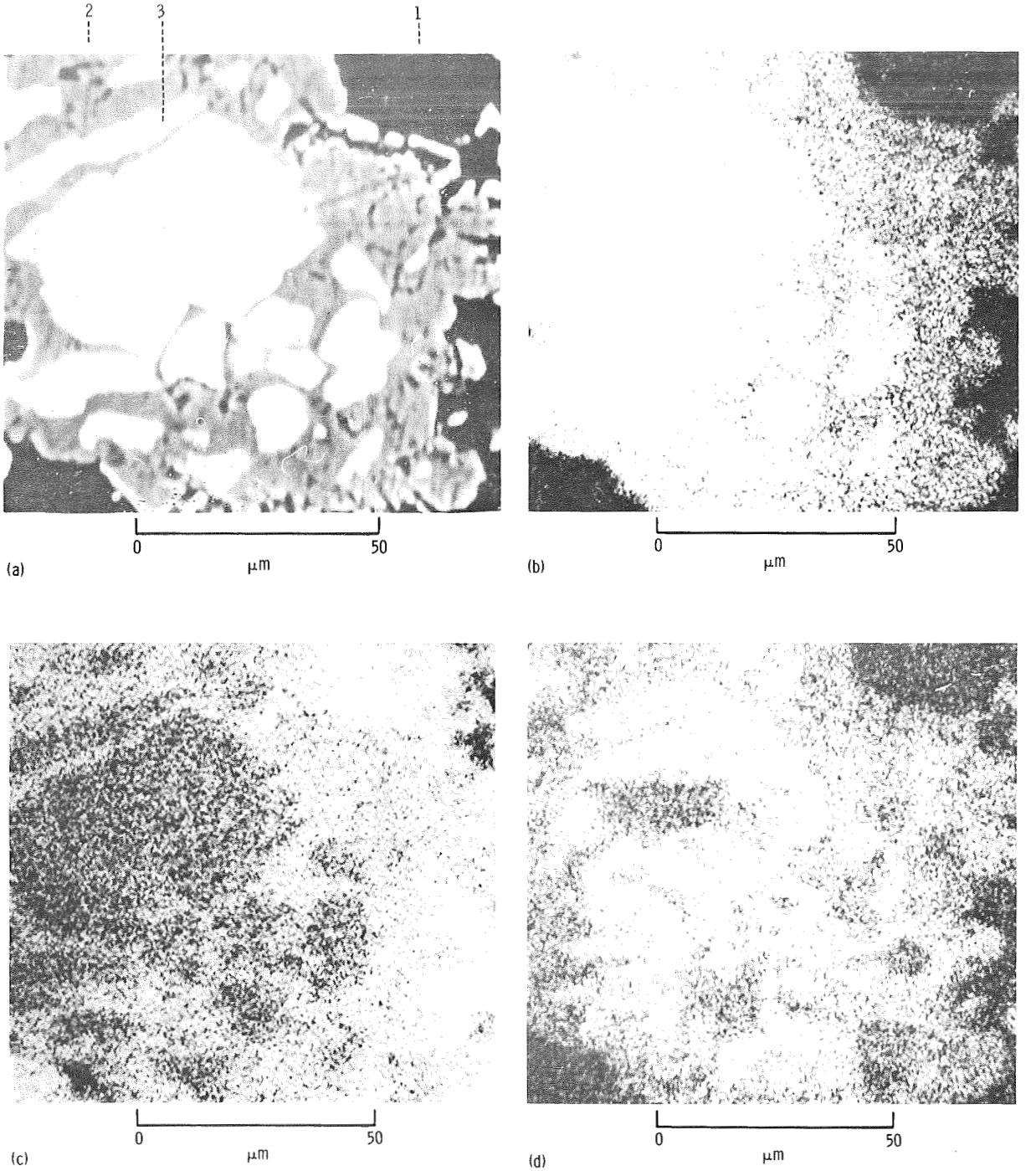


FIGURE 28-29.—Scanning of flight sample MA-150-16 in sectioned areas containing two phases of the W-Al-Re system. (a) Electron beam scanning ("1" indicates the Al, "2" indicates the Al-rich phase (31W 66Al 3Re), and "3" indicates phase 58W 37Al 5Re (table 28-II)). (b) Tungsten Lα radiation. (c) Aluminum Kα radiation. (d) Rhenium Lα radiation.

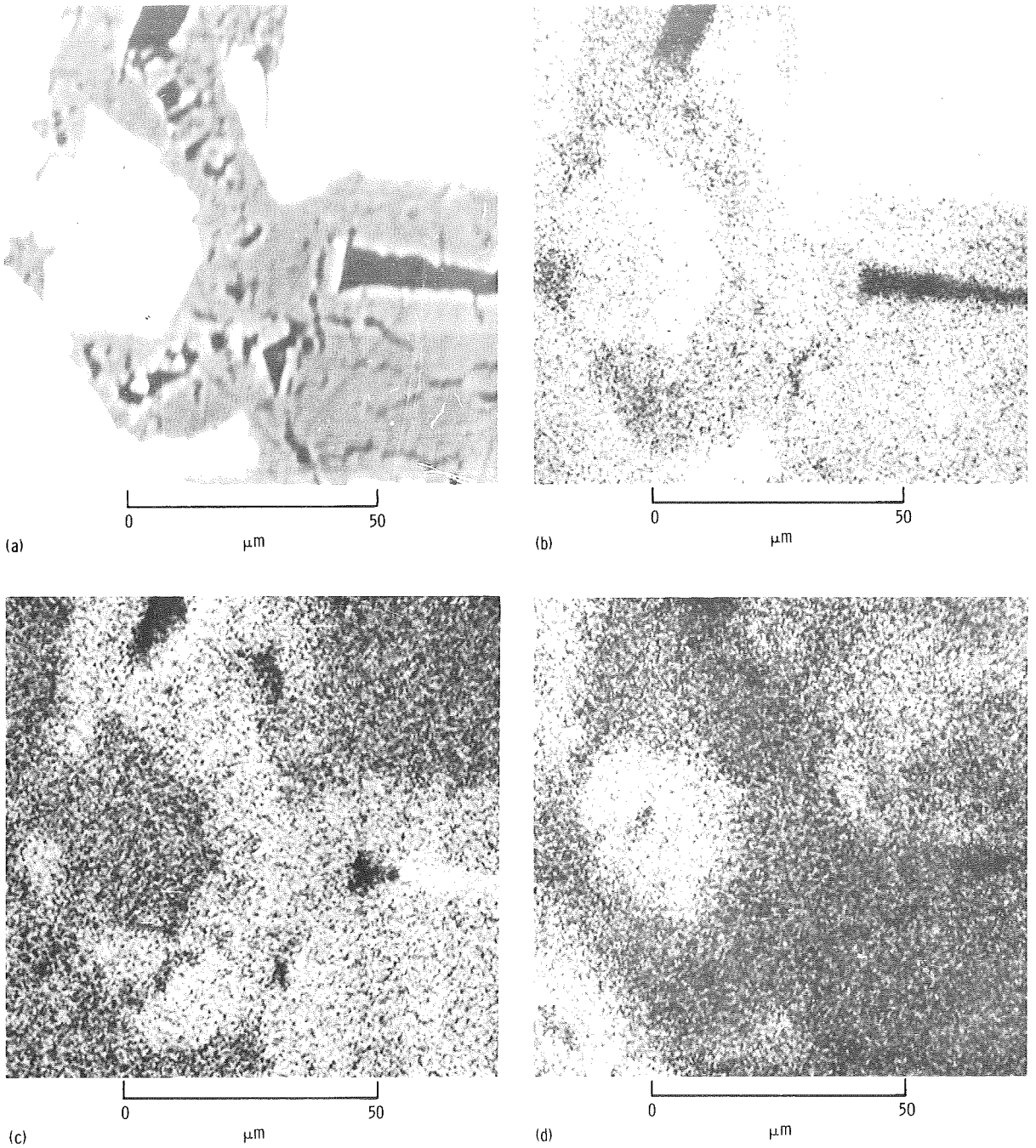


FIGURE 28-30.—Scanning of flight sample MA-150-16 in sectioned areas containing two phases of the W-Al-Re system. (a) Electron beam scanning ("1" indicates the Al, "2" indicates the Al-rich phase (31W 66A1 3Re), and "3" indicates phase 56W 37Al 7Re (table 28-II)). (b) Tungsten Lα radiation. (c) Aluminum Kα radiation. (d) Rhenium Lα radiation.

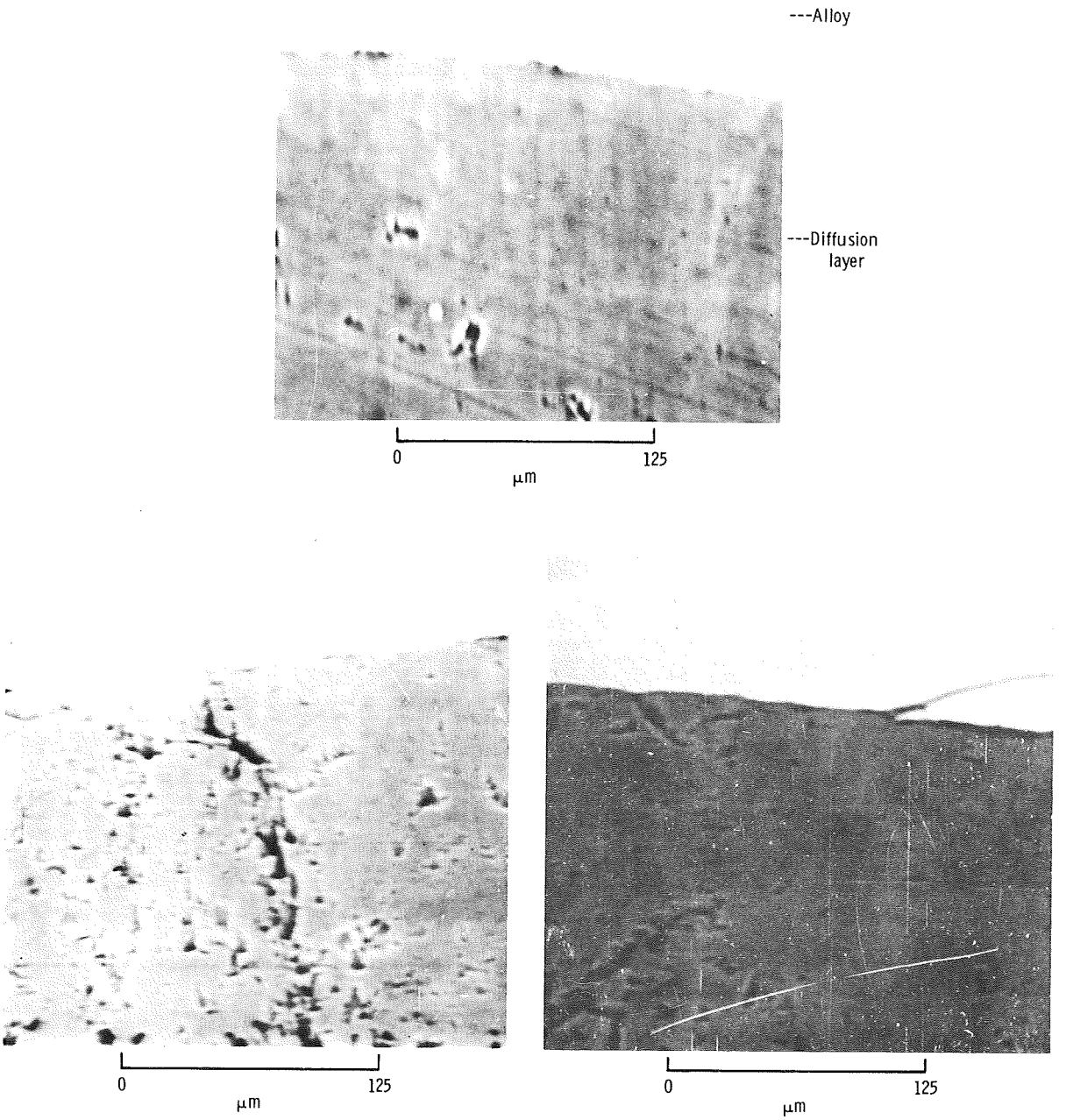


FIGURE 28-31.—Electron beam scanning in different areas of the diffusion layer/WRe alloy interface in ground sample MA-150-11. Pores can be seen in some areas of the diffusion layer.

(wt%). This composition was not observed in the matrix of any other sample (except for the diffusion layer).

Study of the Al/alloy interface revealed that some areas of the diffusion layer are more porous than others (figs. 28-31 and 28-32), the average size of the pores being generally larger in the flight samples. Concentration of pores at the boundary of the diffusion layer and the alloy in flight samples (fig. 28-32) is higher than in ground samples (fig. 28-31).

For further comparison, it should be noted that no appreciable pore formation was observed in the diffusion area between pure W and Al. An increased pore formation was also observed in the Al matrix of the flight ingot.

Microhardness was determined for the WRe alloy, for the Al, and for the diffusion layer phases. The results, summarized in table 28-III, shows the microhardness values of the ground-based sample to be in good agreement with those of the flight sample. The phase in the diffusion layer contiguous to WRe alloy has the highest hardness.

The ingot Al matrix was analyzed for W, Re, carbon, and oxygen content. The first three elements were not detected in dissolved state in any of the samples. Oxygen content, both in flight and ground-based samples, did not exceed the values corresponding to Al surface oxidation resulting from section preparation.

To evaluate the degree of interaction between liquid Al and the graphite crucible walls, carbon and Al distribution across the Al/crucible contact area was determined. The results provide no evidence of any appreciable interaction between the ingot and the crucible for all examined specimens.

### Aluminum Powder and CuAl Eutectic

In ground-based and flight experiments, Al powder was molded into ingots with almost identical outward appearances (fig. 28-33). Samples had low cohesive strength and damaged easily. This was especially true with flight samples. The disintegration of one such sample into small fragments can be seen in figure 28-33(b). This physical characteristic hindered sample examination. Only scanning microscopy made the quantitative analysis of samples possible. The analysis results for the appropriate ingot sections, presented as

*TABLE 28-III.—Microhardness Measurement Results for WRe Alloy, Al, and Diffusion Layer Phases*

| *Specimen* | *Phase* | *Microhardness H, kg/mm²* |
|---|---|---|
| MA-150-11 (ground-based) | WRe alloy | 550 |
| | Al matrix | 21 |
| | Phase bordering with alloy[a] | 645 |
| | Phase bordering with Al[a] | 550 |
| MA-150-16 (flight) | WRe alloy | 550 |
| | Al matrix | 21 |
| | Phase bordering with alloy | 650 |
| | Phase bordering with Al | 550 |

[a]See figure 28-24.

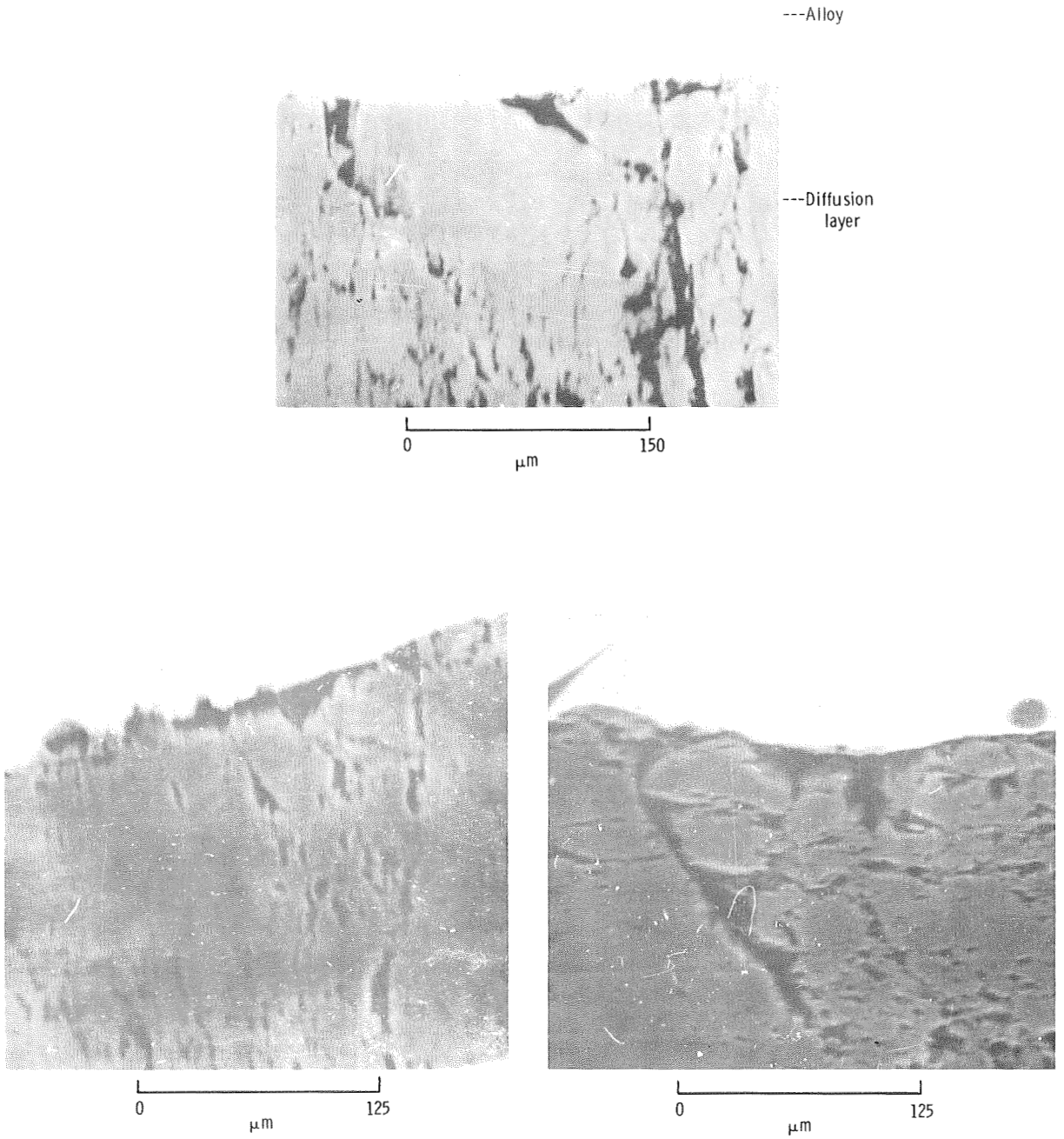


FIGURE 28-32.—Electron beam scanning in different areas of the diffusion layer/WRe alloy interface in flight sample MA-150-16. Pores can be seen at the interface and deep in the diffusion layer.

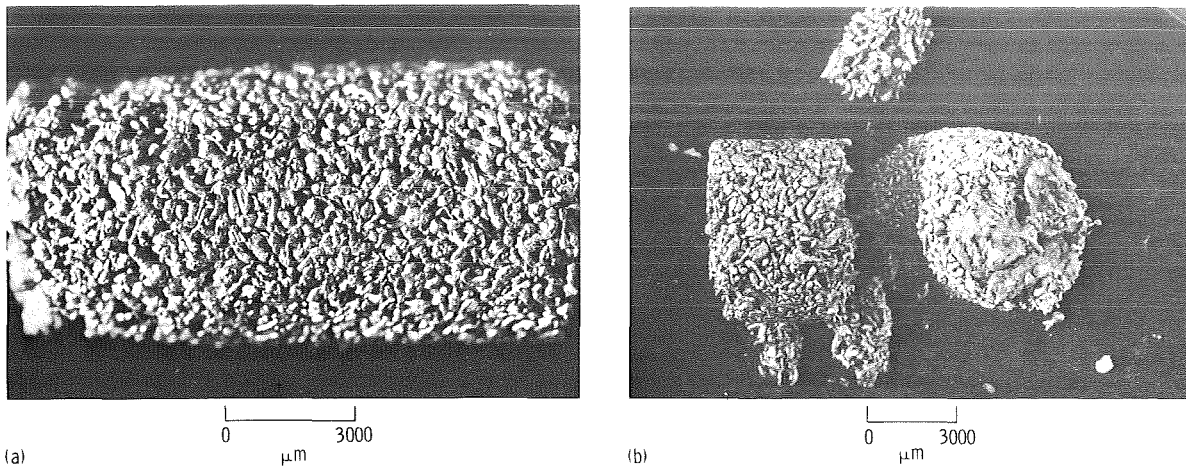


FIGURE 28-33.—Powdered Al sample after the experiment. (a) Ground-based sample. (b) Flight sample.

photographs in figure 28-34, show no evidence of differences between the flight and ground-based samples.

The aluminum foil used to insulate the Al powder from the pieces of eutectics melted completely. Close to the foil, the space- and Earth-grown ingots are somewhat smaller in diameter (fig. 28-33). Fragments of the CuAl eutectic, which in the beginning of the experiment were placed on the bottom of the graphite crucible, failed to melt into one ingot under any experimental conditions. Only a partial fusion of fragments to each other and to the aluminum foil occurred.

The results of metallographic analysis performed on Earth- and space-processed ingots indicate that their original microstructure (laminated eutectic) was not preserved. In both cases, the structure that was formed after melting and subsequent crystallization was composed of $\alpha$-solid-solution (Al-based) and second-phase inclusions. This phase, both in flight and ground-based specimens, occurred in small amounts, generally as isolated elongated inclusions.

Figures 28-35 to 28-38 are photographs of sectioned areas containing $\alpha$-solid-solution and second-phase inclusions. The photographs were made with electron beam scanning and characteristic Cu K$\alpha$ and Al K$\alpha$ radiation. It is apparent that the results for ground-based and flight samples are very similar.

Quantitative X-ray spectral analysis revealed that the phase Cu content for both ground-based and flight samples constituted $\approx$33 at.% (corresponding to the $CuAl_2$ phase), and that Cu content in $\alpha$-solid-solution was within the range of 1.5 to 2 at.% These results are congruent with the Cu-Al system phase diagram data (ref. 28-6).

## RESULTS AND DISCUSSION

### Compound Material

Different reasons for change in the primary structure of ingots (fig. 28-1) after ground-based and flight-based experiments (fig. 28-7) are discussed in this section. In the first case, two different reasons for displacement of W and alloy are evident: (1) marked difference in specific weight between W (WRe alloy) and Al and, consequently, strong gravitational force and buoyancy exerted on the samples by liquid Al melt, and (2) the effects of liquid Al surface tension.

Different effects of these forces can best be illustrated by comparing the location of the W balls and the rod in the alloy. The rod remained at the

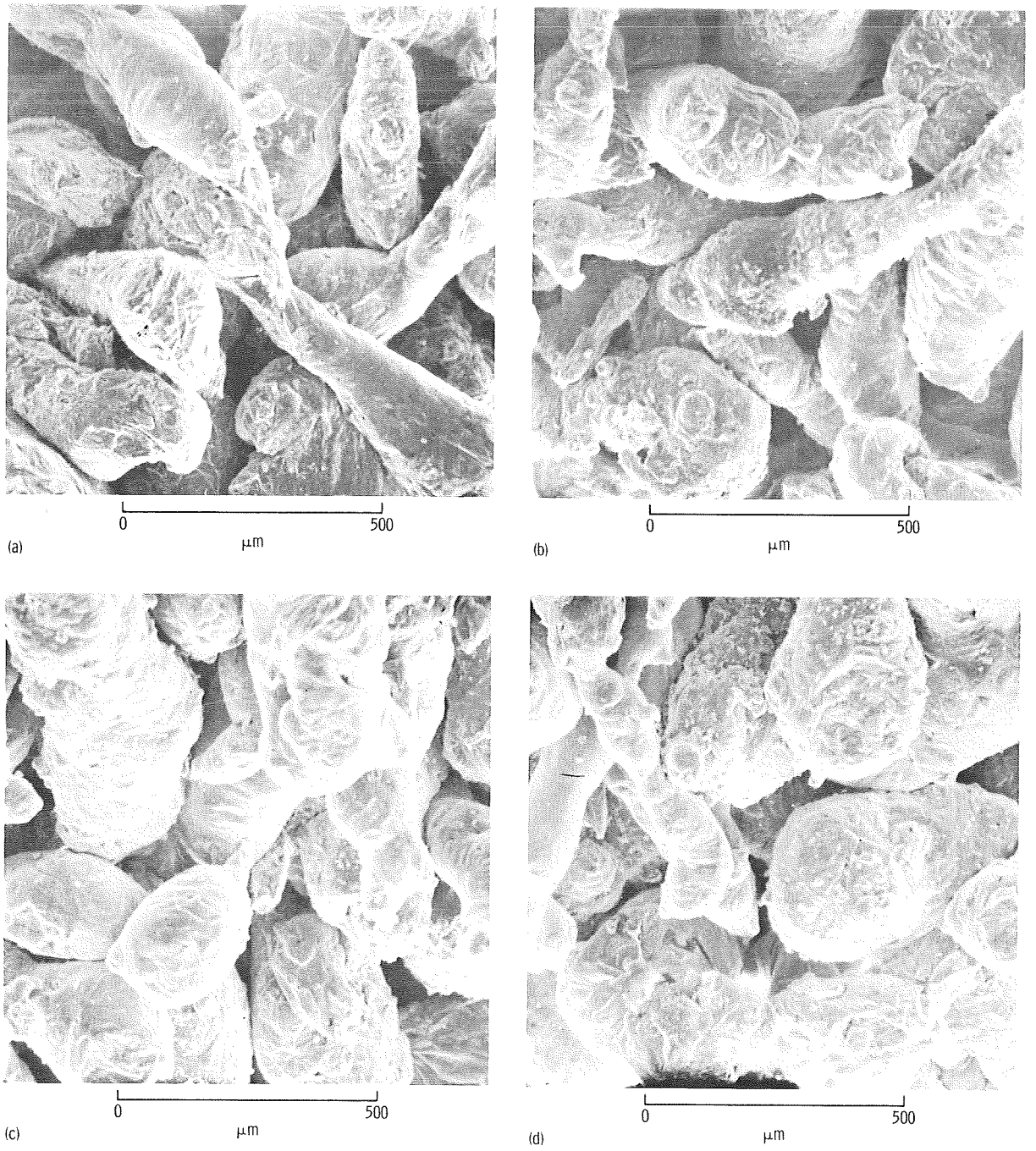


FIGURE 28-34.—Different surface areas of the powdered Al sample. (a) Ground-based experiment (example 1). (b) Ground-based experiment (example 2). (c) Flight experiment (example 1). (d) Flight experiment (example 2).

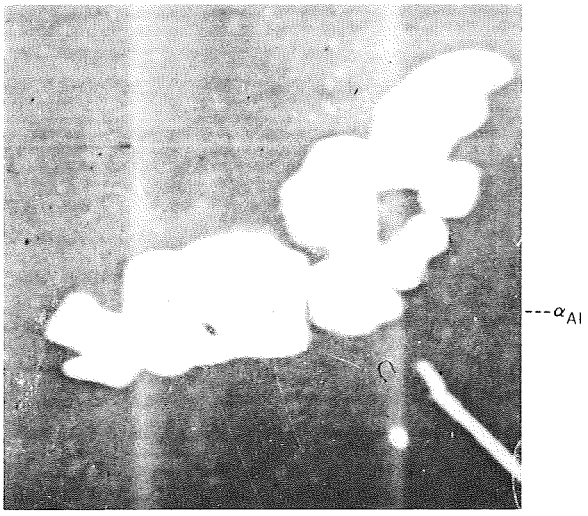


(a)

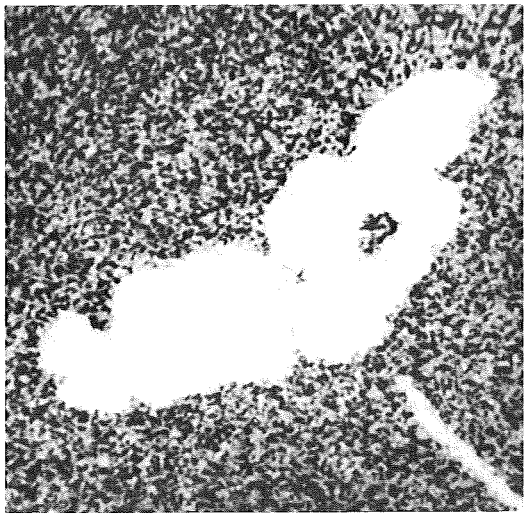

(b)

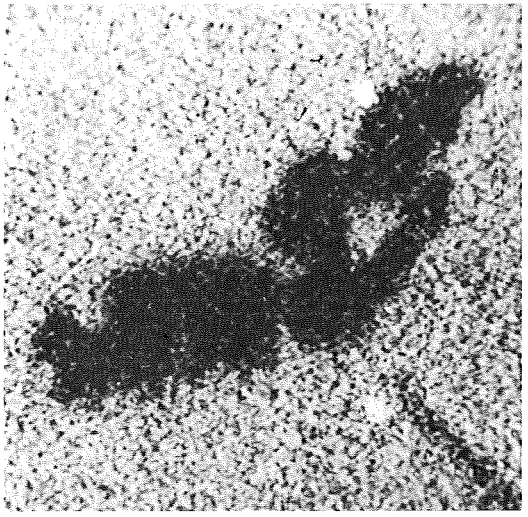

(c)

0 50

μm

FIGURE 28-35.—Scanning of ground-based sample MA-150-9 in areas containing the $\alpha_{Al}$ solid solution and $\theta$ phase of the Cu-Al system. The $\theta$ phase is in the center. (a) Electron beam scanning. (b) Copper K$\alpha$ radiation. (c) Aluminum K$\alpha$ radiation.

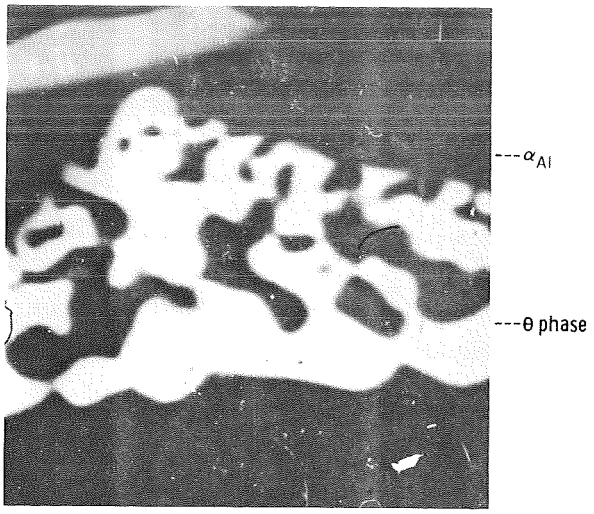


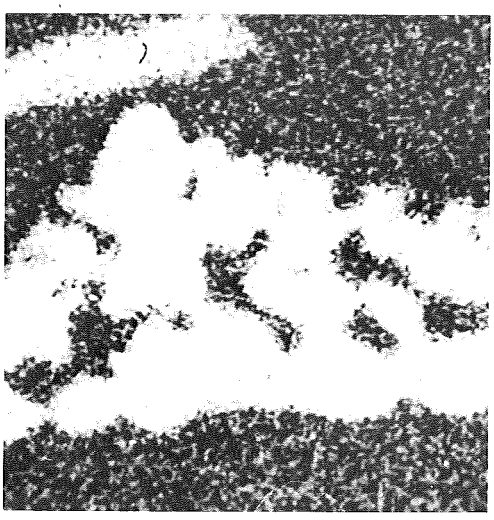


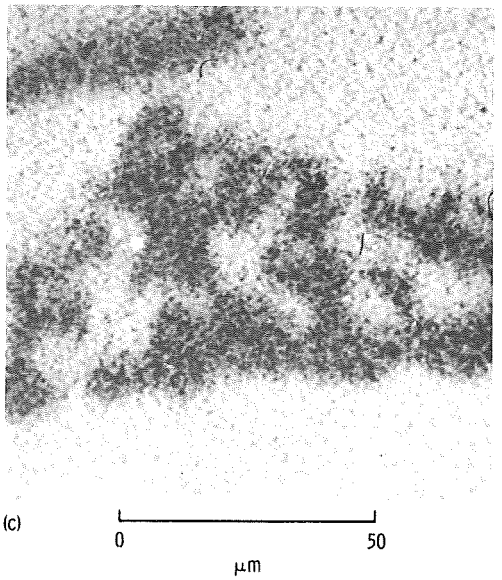


FIGURE 28-36.—Scanning of flight sample MA-150-17 in sectioned areas containing the $\alpha_{Al}$ solid solution and $\theta$ phase of the Cu-Al system. (a) Electron beam scanning. (b) Copper K$\alpha$ radiation. (c) Aluminum K$\alpha$ radiation.

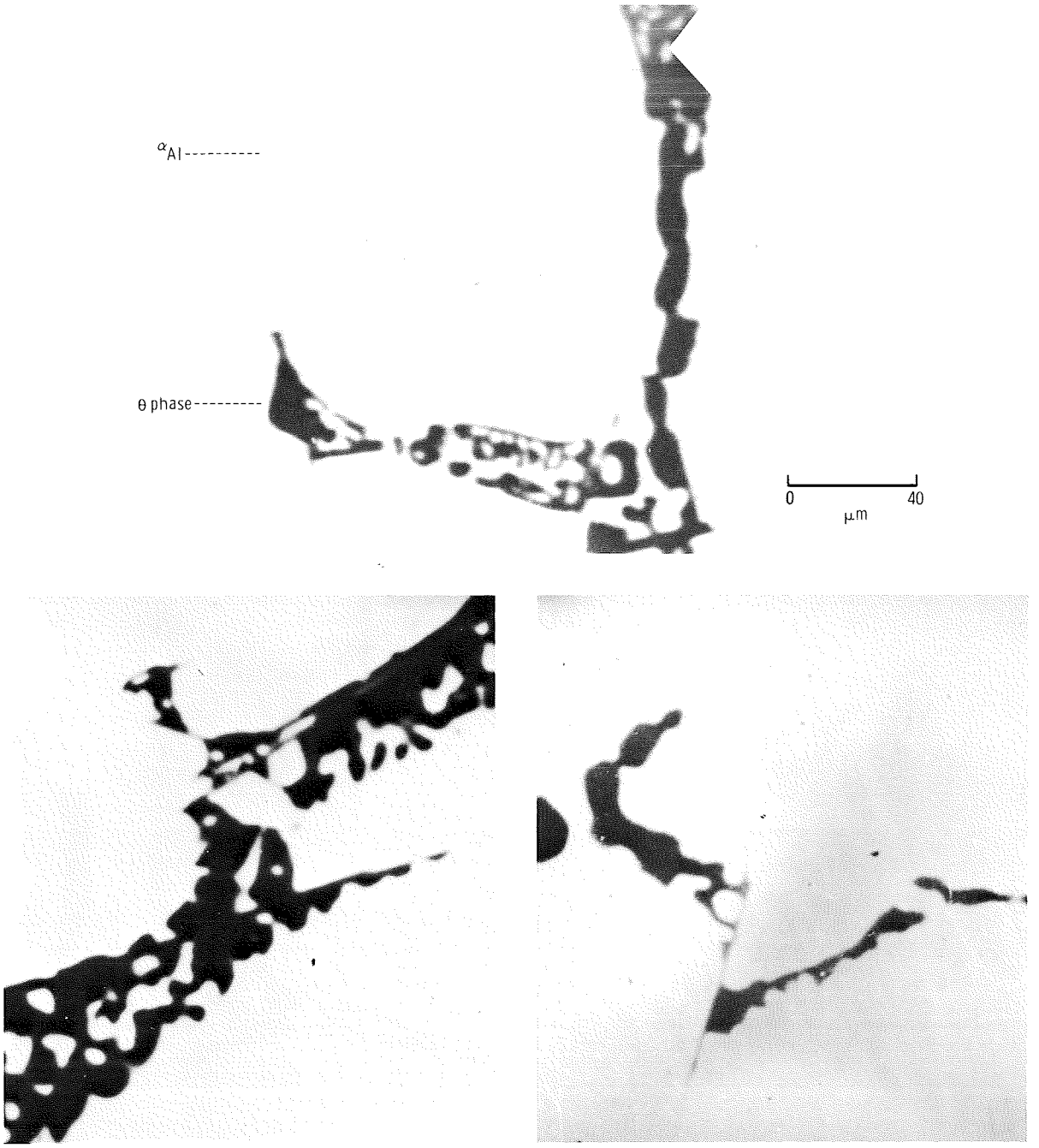


FIGURE 28-37.—Scanning electron photomicrographs of ground-based-sample regions containing the $\theta$ phase of the Cu-Al system.

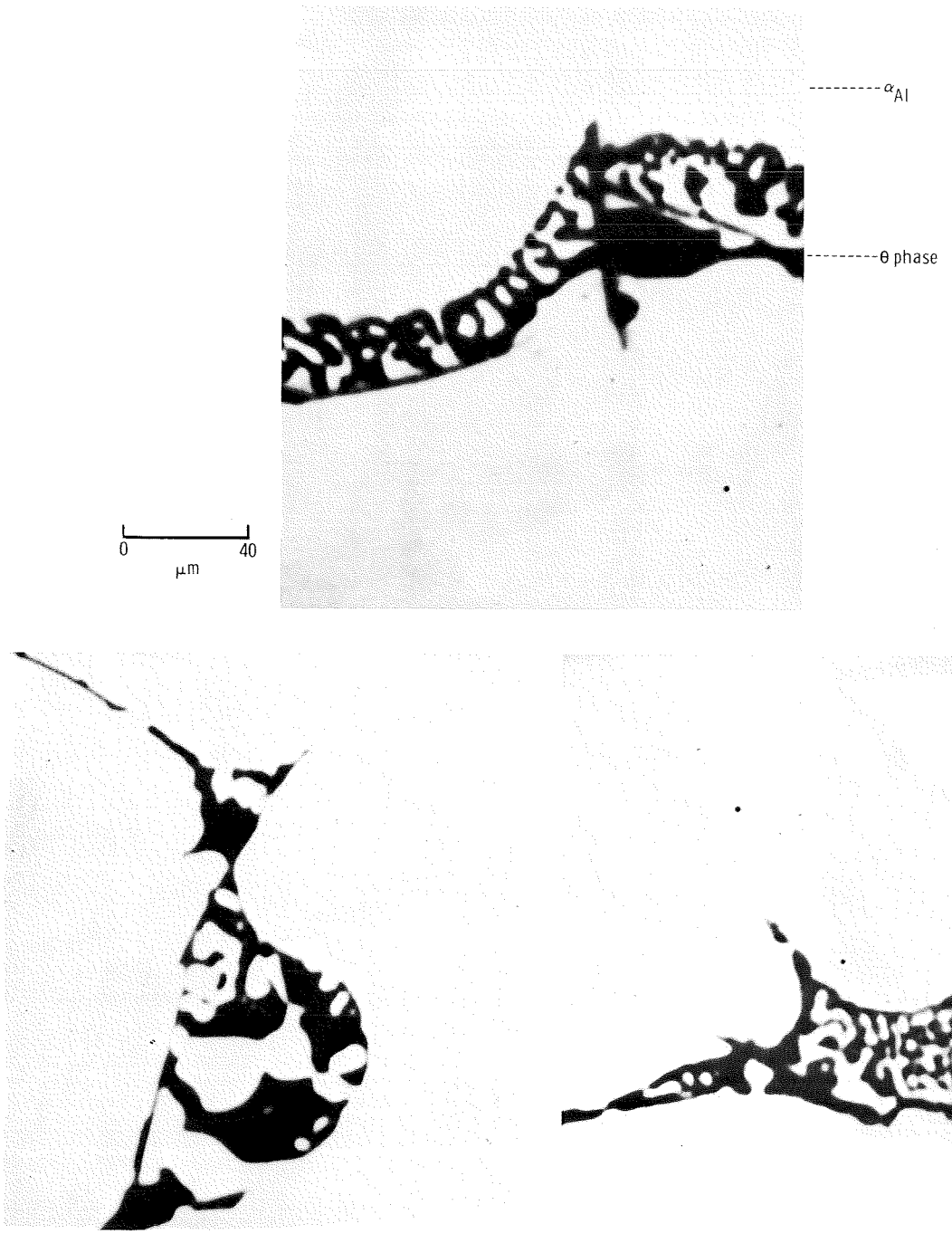


FIGURE 28-38.—Scanning electron photomicrographs of flight-sample regions containing the $\theta$ phase of the Cu-Al system.

surface (fig. 28-7(a)), whereas the W balls shifted to the bottom. Because the rod was initially located at the ingot surface, it was primarily affected by the Al surface tension; however, deeper in the ingot, the effect of this force on W specimens was quite negligible (symmetry conditions). Also, ingot structural formation could have been strongly affected by the Al melt convection and by the interaction between "composite" system constituents. However, in an "ideal" weightless environment, the effects of gravity and buoyancy should be eliminated and melt convection should be brought to a minimum. Under these conditions, it would be only natural to expect that the predetermined structure of the ingot would remain unchanged.

However, gravitation data for the flight-based multipurpose furnace experiment provide ample evidence that weightlessness during the Apollo-Soyuz Test Project (ASTP) was not "ideal." First, the center of gravity of cartridges and ampoules was not coincident with that of the docked spacecraft. Hence, the specimens were subjected to an acceleration force (ref. 28-8) on the order of $10^{-5}$g. Moreover, NASA data indicate that the specimens in ampoules were periodically exposed to accelerations of $10^{-3}$g during spacecraft attitude correction and to $10^{-5}$g acceleration during spacecraft braking. Burn time was within 0.01 to 0.1 second, and the acceleration vector was approximately in the plane perpendicular to the ampoule axis (its direction was not constant).

The possibility of W balls being displaced from their original position as a result of the aforementioned gravity is discussed here. The W/Al interaction, convection of melt, and possible shape changes of the melt will be disregarded.

Assuming that W specimens are shaped as perfect balls, the motion equation for one ball is

$$m\mathbf{a} = \mathbf{F}_{\text{gravity}} + \mathbf{F}_{\text{viscosity}} + \mathbf{F}_{\text{buoyancy}} \qquad (28\text{-}9)$$

where $m$ is the ball mass; $\mathbf{a}$ is the ball acceleration; and $\mathbf{F}_{\text{gravity}}$, $\mathbf{F}_{\text{viscosity}}$, and $\mathbf{F}_{\text{buoyancy}}$ are the flight gravity, viscosity, and buoyancy forces, respectively. Considering that all these forces act along one straight line and designating the flight gravitational acceleration as $g_o$, equation (28-9) can be written as a scalar equation by substituting appropriate values

$$m\frac{d^2x}{dt^2} = mg_o - 6\pi\eta R\frac{dx}{dt} - \frac{4}{3}\pi R^3\rho g_o \qquad (28\text{-}10)$$

where $\mathbf{F}_{\text{gravity}} = mg_o$, $\mathbf{F}_{\text{viscosity}} = -6\pi\eta R\,dx/dt$ (along the slope), $\mathbf{F}_{\text{buoyancy}} = -4/3\pi R^3\rho g_o$, $R$ is the ball radius, $\eta$ and $\rho$ are the viscosity factor and melt density at experiment temperature, respectively, $x$ is the displacement, and $t$ is the time. Direction of flight-induced gravity is taken here as a positive direction.

Equation (28-10) can be rewritten as

$$\frac{d^2x}{dt^2} + \alpha\frac{dx}{dt} + \beta = 0 \qquad (28\text{-}11)$$

assuming that

$$\alpha = \frac{9\eta}{2R^2\rho_{\text{W}}}, \quad \beta = g_o\left(\frac{\rho}{\rho_{\text{W}}} - 1\right) \qquad (28\text{-}12)$$

where $\rho_{\text{W}}$ is the tungsten density.

Of course, no displacement of balls occurs in the absence of gravity. Hence, the initial condition can be written as

$$t = 0,\ x = 0, \frac{dx}{dt} = 0 \qquad (28\text{-}13)$$

Solving differential equation (28-11) for these initial conditions, one obtains

$$\frac{dx}{dt} = \frac{\beta}{\alpha}\left(e^{-\alpha t} - 1\right) \qquad (28\text{-}14)$$

$$x = -\frac{\beta}{\alpha}\left(\frac{1}{\alpha}e^{-\alpha t} + t - \frac{1}{\alpha}\right) \qquad (28\text{-}15)$$

These results can also be valid for a one-g environment, substituting gravitational acceleration

$g_o$ by Earth gravity g. When condition $\alpha t << 1$ in equation (28-15) is met, expanding the exponent into series and restricting calculations to the term of the second order of smallness for $\alpha t$, the displacement $x$ can be written as

$$x = -\frac{\beta t^2}{2} = \left(1 - \frac{\rho}{\rho_W}\right)\frac{g_o t^2}{2} \qquad (28\text{-}16)$$

This equation defines the law that governs displacement of a spherical body as a function of time. It differs from the standard law of uniformly accelerated motion (when the initial velocity is zero) by the presence of the coefficient $1 - (\rho/\rho_W)$ that considers the "buoyancy" effect of the melt. Melt viscosity in these conditions has no effect on the body displacement.

It can be proven that condition $\alpha t << 1$ during the flight-based multipurpose furnace experiment was satisfied only when $t$ was the duration of one "accelerating" impulse. As previously implied, $t_{max} \approx 0.1$ second; $R \approx 5 \times 10^{-2}$cm; $\rho_W \approx 19.3$ g/cm$^3$ (ref. 28-9); and $\eta \approx 1.4 \times 10^{-6}$g/cm sec (ref. 28-10) for $T \approx 1073$ K (800° C). Hence, $\alpha \approx 1.3 \times 10^{-4}$ sec$^{-1}$ and $\alpha t_{max} \approx 10^{-5} << 1$.

Thus, equation (28-16) is valid for the impulse gravity conditions and allows an estimation of $x$ for the duration of one impulse. Displacement of a W ball during one impulse at acceleration $g_o \approx 4 \times 10^{-3}$g $\approx 3.9$ cm/sec$^2$ ($10^{-5}$g acceleration can be disregarded), which is the most common force involved in a spacecraft attitude correction maneuver, will now be determined. Considering that $\rho \approx 2.3$ g/cm$^3$ (ref. 28-10), equation (28-16) gives $t_{min} = 0.01$ second, $x \approx 1.7$ $\mu$m, $t_{max} = 0.1$ second, $x \approx 170$ $\mu$m. Thus, the ball displacement value (in order of magnitude) as a function of impulse duration is within the range of $1\ \mu m \leq x \leq 200\ \mu m$.

It must be emphasized that this calculation is an approximation only and that it applies primarily to the stage immediately following Al melting, during which the interaction between W and Al is still negligible. More rigorous analysis is needed for subsequent stages because of the potential formation of liquid solution of W in the Al (hence, changes in $\rho$ and $\eta$ ) and because of the growth of intermetallic phases between W and Al (i.e., continuous changes in mass and shape of a moving body).

The analysis results suggest that gravitation in flight experiments may cause a displacement of W balls (figs. 28-7(b)) during the initial stages of the solid and liquid metal interaction. However, displacement of specimens in subsequent stages may also result from the phase growth interaction of the adjacent specimens and possibly from the microgravity-induced convection and shape changes of the ingots.

As was noted previously, a composite, microgravity-melted ingot is larger than its ground-melted counterpart. Such an increase in size may be attributed to the fact that the air, which is absorbed by the Al and which fills the gaps in the material interface, cannot be completely removed from the melt in a microgravity environment (unlike on Earth); it remains trapped in the melt, causing an increased macroporosity of aluminum and a "swelling" of the ingot. An estimation of possible air-bubble displacement occurring in the melt under the influence of flight gravitation can serve as confirmation of this fact.

The relationship in equation (28-15) can be valid for any spherical inclusion affected by the above forces (eq. (28-9)). Assuming the air density of $\rho_B \approx 10^{-3}$ g/cm$^3$ (eq. (28-10)), then equation (28-12) proves that the condition $\alpha t >> 1$ (where $t$ is the duration of an acceleration pulse) was always satisfied for bubbles having a diameter of 1 to 100 $\mu$m. The inequality obtained indicates $t >> 1/\alpha$, and all the more for $t >> \frac{1}{\alpha} e^{-\alpha t}$. Therefore, for bubble displacement in the melt, equations (28-12) and (28-15) give

$$x = -\frac{\beta t}{\alpha} = -\frac{2R^2}{g}\frac{(\rho - \rho_B)}{\eta} \qquad (28\text{-}17)$$

Since $(\rho - \rho_B) > 0$, the minus on the right side of equation (28-17) indicates that the bubbles are displaced in the direction opposite to that of the flight gravitation force, which always occurs under one-g conditions as well.

Based on equation (28-17), table 28-IV shows estimations of the maximum value of bubble displacement occurring during one impulse $t_{max}$ = 0.1 second for $g_o \approx 4$ cm/sec$^2$. The table indicates

*TABLE 28-IV.—Estimates of Bubble Displacement*

| *Bubble diameter, μm* | *Maximum value of displacement, μm* |
|---|---|
| 1 | 5 |
| 10 | $5\times10^2$ |
| 100 | $5\times10^4$ |

that the displacement of bubbles with a diameter of no more than 100 μm did not exceed the mean size of the Al ingot. The presence of such bubbles obviously caused an accumulation of macropores in the bulk of the ingot as well as in the area of the diffusion/alloy interface in the flight sample (fig. 28-32).

## Tungsten and Tungsten-Rhenium Alloy/Aluminum Interaction

General physical considerations suggest that, given the temperature of the flight and ground-based experiments, a process of mutual diffusion should occur between solid W and liquid Al. This process should result in the formation of intermediate phases within the diffusion layer, as predicted by the W-Al system constitutional diagram. Furthermore, liquid solution of W may form in the Al as a result of this diffusive interaction (fig. 28-14).

Results of the experiments indicate that three phases were indeed observed, but that each phase was formed under specific circumstances. Thus, the $WAl_4$ phase can develop practically at any experimental temperature. On the other hand, the $WAl_5$ phase (see constitutional diagram in fig. 28-14) can exist only at temperatures below 1143 K (870° C). Consequently, the $WAl_5$ phase developed only during the experiment cooldown specimen, which lasted approximately 1 hour (fig. 28-5).

The markedly greater thickness of the $WAl_5$ phase as compared to the $WAl_4$ phase, despite the much longer formation time of the latter, can be explained by the fact that the $WAl_4$ phase growth occurs at temperatures far below its melting point (1599 K (1326° C)), whereas the $WAl_5$ phase grows at temperatures close to its melting point. It is not unlikely that the $WAl_5$ phase grows at the expense of the $WAl_4$ phase by means of "diffusive dilution."

Finally, the third phase ($WAl_{12}$), which exists at temperatures below 970 K (697° C) (fig. 28-14), could grow in the diffusion layer no longer than ≈15 minutes after the temperature was lowered (fig. 28-5). Hence, its "diffusion" area thickness was very small and in some places impossible to detect.

Another phase formation mechanism to be considered other than diffusion is the precipitation of phases from liquid solution in the process of cooling. This mechanism may, for example, explain the inhomogeneous distribution (fig. 28-15(b)) and the varied thickness of the phases throughout different areas of the Al/W interface. Perhaps the crystalline faceting of the $WAl_{12}$ phase in the flight sample can be also attributed to the $WAl_{12}$ precipitation from the melt under conditions of lower convection than on Earth.

The presence of convection in the space-flight environment, together with Al penetration along grain boundaries into the phases, may explain the formation of small phase fragments in the Al matrix as well as the dendritic growth of these phases. It should also be noted that a division of the diffusion front into elongated and dendritic sections (figs. 28-9 to 28-13) could be related to finite dimensions of W specimens and to the effect this produced on diffusion. In early stages of the process, when specimen dimensions were "semi-infinite" compared to dimensions of the layer, the diffusion front was dense. However, the already limited amount of W became insufficient to sustain such a front, which soon began to disintegrate. At this stage, the process developed

radially (figs. 28-9 to 28-13). Lower convection of melts in a microgravity environment could be also responsible for the somewhat lower "disorientation" of the needlelike parts of the layer in flight specimens as compared to ground-based specimens (figs. 28-16 to 28-19).

The diffusive reaction between Al and WRe alloy will now be discussed. Analysis has shown that the process of mutual diffusion between solid alloy and liquid Al occurs both in microgravity and one-g environments. As a result, two intermetallic phases (figs. 28-23 and 28-24) of short concentration range are formed in the diffusion layer. Division of the layer into single elongated sections, which is typical of the W-Al system, was not observed. This may be associated with the fact that the starting alloy sample in the experimental temperature/time mode was "semi-infinite" with respect to the diffusion layer thickness.

Similar concentration curves for the distribution of constituents in ground-based and flight samples indicate that microgravity phase formation in the diffusion layer is subject to the same laws as in a one-g environment. However, the lack of reliable structural diagrams for the W-Al-Re system hinders more detailed evaluation. Especially, it does not seem possible to establish the extent to which the boundary concentrations in the diffusion layer phases correspond to the constitutional-diagram-predicted values. Particularly interesting in this respect is the boundary of the W-richest phase and Al. Both in ground-based and flight samples (fig. 28-24), an appreciable increase in W concentration and a decrease in Re concentration (Al content changes are small) were simultaneously noted as one approaches this boundary and becomes farther from the center of the phase. However, how close the boundary concentrations are to the equilibrium values for the specimens studied is unknown.

Equally difficult to explain is the formation of numerous individual fragments of W-Al-Re system phases (figs. 28-25 to 28-30) in the Al matrix. Two mechanisms explaining their formation can be tentatively offered: (1) phase precipitation from the solution in the process of cooling (if the constitutional diagram predicts the existence of such a solution within the experimental temperature range) and (2) separation of phase crystals from the diffusion layer resulting from grain-boundary diffusion of Al into the phase and from gravity induced convection of the melt.

When the first mechanism is the predominant one, then a structural analysis of phases precipitated from the solution (table 28-II) and of phases grown in the diffusion layer (fig. 28-24) permits an assumption that three phases are present in the W-Al-Re system for the studied temperature range. These phases should have different melting points $T_{melt}$, and their boundary concentrations should be a function of temperature. It follows that the Al-richest phase (more than 60 wt%), detected only in flight specimen MA-150-16 (table 28-II), has the lowest $T_{melt}$ value.

However, if the second mechanism predominates, then the absence of liquid solution might suggest the occurrence of a diffusion of Al from the melt into phase fragments that separated from the layer. The formation of phases with increased Al content in flight samples indicates more intensive diffusion of Al in a microgravity environment. However, more experiments are needed before reliable interpretation of these results can be made.

Results obtained from measuring microhardness $H$ for different phases of the W-Al and W-Al-Re system will now be discussed briefly. An agreement in $H$ values for the aforementioned systems in ground-based and flight samples (tables 28-I and 28-II) indicates microstructural similarity of the Earth- and space-grown phases. As far as the Al matrix is concerned, the "swelling" of flight-processed melts stems from macroporosity, a fact mentioned previously. The greatest hardness value in the W-Al-Re system is found in the phase having the highest content of Re (fig. 28-24, table 28-III). Of all phases tested for microhardness in the W-Al system, the $WAl_5$ phase located in the diffusion layer was found to have the highest values of $H$. However, individual "needles" of the $WAl_5$ phase have somewhat lower hardness values (table 28-I). This discrepancy may be associated with the fact that the $WAl_5$ phase located in the diffusion layer exists within a certain concentration range (allowable by the W-Al system constitutional diagram) and is richer in W than the more homogeneous individual "needles" of this phase.

### Powdered Aluminum and Eutectics

Analysis of results reveals that fusing of powder particles (fig. 28-34) in flight and ground-based samples did not occur. This may be attributed to the fact that each Al particle is protected by an oxide coating, the melting point $T_{melt}$ of which is considerably higher than that of pure Al. The presence of this coating prevented interparticular fusing, although pure Al melting ($T_{melt}$ = 933 K (660° C)) within each particle in the studied temperature range (fig. 28-5) did occur in both flight and ground-based specimens.

The possibility of particles becoming "coupled" in certain areas was higher in the more constant (in value and direction) Earth gravity than in the much lower and more variable orbital gravity. This was a factor that determined the somewhat higher cohesive strength of the ground-processed powdered ingots as compared to the flight-processed ingots.

Preliminary analysis data on the CuAl eutectic failed to demonstrate any substantial effect of weightlessness on the resultant ingot structure. As previously implied, neither flight nor ground-based specimens maintained the original lamellar structure after melting. This may be associated with the following factors: (1) deviation from the originally predetermined composition and (2) alloy cooling conditions (fig. 28-5).

According to the constitutional diagram (ref. 28-6), the ratio of $\theta$-phase and $\alpha$-solid-solution in a eutectic alloy CuAl should be more or less constant. However, all examined specimens showed higher $\alpha$-solid-solution content. This is probably associated with the aluminum foil dissolving in the alloy and the resultant change in the chemical composition of the alloy.

As is well known, cooling conditions can strongly affect the formation of an eutectic microstructure (ref. 28-11). In these experiments, the temperature/time mode led to phase separation and to the disappearance of the original lamellar structure (figs. 28-35 to 28-38).

It should be noted that the Cu content in $\alpha$-solid solution (1.5 to 2 at.%) for both types of specimens was higher than normally expected at room temperature and as predicted by the Cu-Al system constitutional diagram. This supersaturation of the solution may be attributed to a rapid cooling of the alloy from 773 K (500° C) (fig. 28-5), a temperature at which the solubility of Al and Cu corresponds to the above values.

## CONCLUSIONS

The results of this preliminary analysis justify a conclusion that, despite a low-g environment onboard the spacecraft, the predetermined distribution of refractory inclusions in composite material was not maintained after the matrix was melted. This may be attributed to the effect of gravity onboard the spacecraft and to the interaction between different constituents of the composite material.

The Al matrix of the space-grown ingots is more porous than it is in Earth-grown ingots. Space-grown ingots are also larger and shaped differently than Earth-grown ingots.

The kinetics of diffusion and phase formation in the solid W (WRe alloy)/liquid Al diffusion area was approximately the same for both ground-based and flight samples. This is evidenced by the similarity in geometrical characteristics of the compared diffusion layers as well as by the analogous phase composition and distribution of the diffusion layer constituents.

At the same time, microgravity diffusion and phase formation processes for the W-Al and W-Al-Re systems exhibit some striking differences. In the binary system, the $WAl_5$ phases are thinner than on Earth, are needle-shaped, and have a lower disorientation angle; the $WAl_{12}$ phase has a crystalline faceting. In the case of the tertiary system, the distinguishing features include a higher porosity at the diffusion layer/WRe alloy interface, and the formation of phases rich in Al.

Samples of the CuAl eutectics and powdered Al processed under specified temperature/time conditions in space showed no appreciable difference from their Earth-processed counterparts. Experiments with powdered Al demonstrated that a slight excess of temperature above the Al melting point reduces the possibility of individual particles being fused together in a low-gravity orbital environment.

## REFERENCES


28-1. Castaing, R.: Application of Electron Probe to Local Chemical and Crystallographic Analysis. Ph.D. Dissertation, Univ. of Paris, 1951. (Translation by P. Duwez and D. B. Wittry, WAL 142/59-7, Calif. Inst. of Technology, 1955.)

28-2. Borovskii, I. B.; and Rydnik, V. I.: The Theory of Quantitative Electron Probe Analysis. Quantitative Electron Probe Analysis, K. F. J. Heinrich, ed., National Bureau of Standards, Special Publication 298, U.S. Dept. of Commerce (Washington, D.C.), 1968, pp. 35-52.

28-3. Philibert, J.: A Method of Calculating the Absorption Correction in Electron Probe Microanalysis. X-Ray Optics and X-Ray Microanalysis, H. H. Pattee, V. E. Cosslett, and A. Engström, eds., Academic Press (New York), 1963, pp. 379-392.

28-4. Reed, S. J. B.: The Present State of Quantitative Electron Probe Microanalysis. Rev. Phys. Technol., vol. 2, no. 2, 1971, pp. 92-115.

28-5. Duncumb, P.; and Reed, S. J. B.: Progress Achieved in Calculating the Stopping Power and the Backscattering Coefficient. Physical Bases for X-Ray Spectral Local Analysis, Nauka Press, 1973, pp. 117-138.

28-6. Hansen, Max: Constitution of Binary Alloys. Second ed., McGraw-Hill Book Co., 1958.

28-7. Gurov, K. P.; Pimenov, V. N.; and Ugaste, Yu. E.: Some Features of Mutual Diffusion in Multiphase System. Physics of Metals and Metallography, vol. 32, no. 1, 1971, pp. 101-107.

28-8. Belyakov, I. T.; and Borisov, U. D.: Technology in Space. NASA TT F-16264, 1975.

28-9. Shultze, G.: Physics of Metals. MIR Press (Moscow), 1971.

28-10. Koshkin, N. I.; and Shirkevich, M. G.: Elementary Physics Manual. FIL Press (Moscow), 1962.

28-11. Maltsev, M. V.: Metallurgy of Industrial Nonferrous Metals and Alloys. JPRS-55357, 1972. (Available from the National Technical Information Service.)